Investigating energy dissipation for a methodology to fatigue master curves

MSc Thesis

by

S. Stikkelorum

TU Delft

Preface

This thesis summarises all the work I have done these past months in order to investigate and understand fatigue in composites. It has been written in order to graduate with a MSc degree in Aerospace Engineering at Delft University of Technology.

I would like to thank my supervisor René Alderliesten for providing me with the feedback and guidance to help me through this process and getting as much as possible from my research. I would also like to thank Dimitrios Zarouchas for giving me advice on acoustic emission.

I also want to take this moment to thank my family and friends for supporting me throughout my education. It has been a tough couple of years with many struggles, but I managed to fight through them with your help.

I hope the research I have done will prove to be insightful and useful for others in the future.

S. Stikkelorum
Delft, 6 February 2019

Summary

Fibre reinforced polymer composites are used in an increasing amount of aircraft structures for weight optimisation. For safety and certification purposes, the fatigue behaviour of these structures have to be predicted. However, most of the current models are phenomenological in nature and lack the relation to the actual physical behaviour and damage growth of composites during fatigue. Recent studies have shown that there is a possible relation between damage growth and energy dissipation, as the amount of energy dissipated during a cycle is related to the damage mechanisms caused by crack extension.

The purpose of this MSc thesis is to investigate the relation between energy dissipation and damage mechanisms in order to develop an analytical method for predicting fatigue life based on the physical behaviour of composites during fatigue.

First, an overview was provided of background information related to damage mechanisms, the current state of the art fatigue life assessment and fatigue life prediction, and energy dissipation. Typical damage mechanisms found in quasi-isotropic open-hole coupons during tension-tension fatigue were matrix cracks in the 90° plies, followed by matrix cracking in the 45° and -45° plies starting from the centre of the hole. Lastly, fibre splitting in the direction of the loading occurs in the 0° plies.
There are no standardised tests for fatigue life assessment for open-hole tension-tension fatigue, however the geometry for tensile static tests could be used for fatigue tests.
For fatigue life prediction most models are phenomenological in nature either based on fracture mechanics, stiffness degradation or finite element modelling.
Energy dissipates in three different forms: mechanical energy, heat and acoustic energy. The mechanical energy dissipated can be determined by calculating the area within the hysteresis loops of the load-displacement curves. The heat can be minimised by testing at lower frequencies and the acoustic energy can be measured using acoustic emission.

Open-hole coupons with four different lay-ups, unidirectional (0°), crossply (0°/90°), angle-ply (45°/-45°) and quasi-isotropic (0°/90°/45°/-45°), were manufactured using hand lay-up with Hexply 8552 prepreg tape and cured according to the manufacturer's specifications in an autoclave.
The coupons were tested for tension-tension fatigue using a MTS 100 kN fatigue test bench at a frequency of 5 Hz and a stress ratio of 0.1. The load cycles during the tests had constant amplitude and were load controlled. The coupons were clamped at both ends and two acoustic emission sensors were clamped to the coupons away from the open hole. During the tests load and displacement data was measured by the test bench during an entire load cycle each 100th cycle. After each 100th load cycle pictures were taken by two cameras for digital image correlation.

The digital image correlation was used to measure the damage growth during the tests. As the coupons were not tested fully until failure, the number of cycles to failure was based on a damage threshold. The crack growth caused by fibre splitting in the 0°plies showed similar behaviour in the unidirectional and crossply coupons, but not in the quasi-isotropic coupons as matrix cracking in the 90°, 45° and -45° plies occurred first. The growth of the matrix crack in the 90° plies could not be recorded, as these cracks reached the edge of the coupon within 100 cycles. In order to improve the measurement of matrix crack growth, the frequency at which pictures are taken during the first 100 cycles could be increased.

Then, the load and displacement data from the test bench were used to calculate the cyclic work and energy dissipated using the area underneath the load-displacement curves. The dissipated energy per cycle was compared with the crack growth, however there does not appear to be a correlation between the two. The cyclic work seems to be related to the damage mechanisms, as the behaviour of the cyclic work differs per lay-up suggesting a relation between displacement and crack growth. Therefore, the relation between displacement and crack length was investigated. This relation was then used to calculate the strain energy release rate, which was compared with the crack growth rate and cyclic work per cycle.

Lastly, the acoustic emission data was used to calculate the cumulative acoustic energy and number of acoustic hits and compared with the crack growth. To see if acoustic features for different damage mechanisms could be identified, the registered rise time, duration and amplitude were plotted and divided based on the loads at which these hits were registered.

In the unidirectional, crossply and quasi-isotropic coupons the cyclic work first have a steep increase, after which the slope decreased. For unidirectional and crossply coupons the slope continued to decrease until an apparent asymptote was reached, while the cyclic work for quasi-isotropic coupons continues to increase over the number of cycles after the change in slope. The cyclic work for the angleply coupons continued to increase with increasing number of cycles without a decrease in slope. Therefore, the continued increase in cyclic work found in the quasi-isotropic can be related to the continued increase found in the angleply coupons, while the steep increase at the start can be due to 0° plies in the quasi-isotropic coupons.
The distribution of dissipated energy over time suggests there is no relation between the damage mechanisms and growth found with digital image correlation and the amount of energy dissipated during a cycle. However, there appeared to be a linear relation between total amount of dissipated energy and number of cycles until failure. The cumulative acoustic energy and number of hits appeared to be related to the crack growth, as the cracks approached the acoustic emission sensors. After investigating the acoustic features it was found that most of the damage growth occurred for loads between 75% and 100% of the maximum load. Damage mechanisms in unidirectional coupons were found to have low rise time, high amplitude and medium to high duration. In crossply coupons the damage mechanisms could be characterised by medium rise time. high amplitude and medium to high duration. In angleply coupons the damage mechanisms were characterised by high amplitude, medium to high duration and low to high rise time. These characteristics could not initially be identified in the quasi-isotropic coupons, most likely due to the large amount of data overlapping. In order to improve relating the acoustic emission features to damage mechanisms, pattern recognition software can be used to analyse the features. The features can also be divided based on time of occurrence instead of loads so it can be compared to measured crack growth.

Contents

Nomenclature

List of abbreviations

Abbreviation	Definition
AE	Acoustic Emission
CZM	Cohesive Zone Model
CFRP	Carbon fibre reinforced polymers
DIC	Digital Image Correlation
FRP	fibre-reinforced polymers
GFRP	Glass fibre reinforced polymers
QI	Quasi-isotropic
SERR	Strain Energy Release Rate
TDE	Total Dissipated Energy
UD	Unidirectional
VCCT	Virtual Crack Closure Technique

List of symbols

List of Greek symbols

Symbol	Definition
$\Delta\sigma_o$	Fatigue limit
δ	Displacement
δ_d	Displacement at which delamination starts
δ_f	Displacement at which failiure occurs
ϵ	Strain
σ	Stress
σ_f	Failure stress
σ_{max}	Maximum stress
σ_u	Tensile strength of the material

List of Roman symbols

Symbol	Definition
A	Amplitude
a	Crack length
a_l	Length of left crack
a_{lb}	Length of bottom left crack
a_{lu}	Length of upper left crack
a_r	Length of right crack
a_{lb}	Length of bottom right crack
a_{ru}	Length of upper right crack
a^*	Crack length
$a^*_{l(45)}$	Length of left crack in 45° direction
$a^*_{l(-45)}$	Length of left crack in -45° direction
$a^*_{r(45)}$	Length of right crack in 45° direction
$a^*_{r(-45)}$	Length of right crack in -45° direction
b	Width
C	Compliance
d	Displacement
d_0	Displacement at which the load is zero
d_{max}	Maximum displacement
d_{min}	Minimum displacement
D	Damage parameters
D	Diameter
E	Modulus of elasticity
F	Load
F_{max}	Maximum load
f	Frequency
G	Strain Energy Release Rate
G_{max}	Maximum strain energy release rate
G_{min}	Minimum strain energy release rate
h	Projected horizontal crack length
h_l	Projected horizontal length left crack
h_r	Projected horizontal length right crack
K_c	Fracture toughness
K_t	Stress concentration
k	Slope of the load-displacement curve
L	Length of the specimen
N	Number of cycles
N_f	Number of cycles until failure
R	Stress ratio
R^2	Curve fitting parameter
t	Time
U	Work
U_1	Work done during the first half of the load cycle
U_2	Work done during the second half of the load cycle
U_{cyc}	Cyclic work
U_d	Dissipated Energy
u	Displacement
u_{max}	Maximum displacement
u_{min}	Minimum displacement
v	Project vertical crack length
v_l	Projected vertical length left crack
v_r	Projected vertical length right crack
w	Width specimen

List of Figures

List of Tables

1

Introduction

The use of composites in aircraft structures is increasing in order to reduce the mass of aircraft. Therefore, models to predict fatigue life have been developed, but most of these models are phenomenological and lack physical meaning. They are unable to fully describe the fracture modes involved during fatigue and are incapable of fully predicting the damage growth.Therefore, airworthiness authorities require that the structures have slow to no growth of damage during their lifetime for an aircraft to be certified. This leads to structures being overdesigned in order to prevent damage growth. Recent studies of fatigue in metals [7, 12, 24, 27, 28], delamination growth in composites [1, 3] and disbonds at adhesive interfaces [36] have indicated that there may be a relation between fatigue and energy dissipation. The amount of energy dissipated is related to the damage mechanisms in the material during crack extension [3], so energy dissipation can be used to relate fatigue life to the damage mechanisms in composites.

The main objective of the thesis is to find a relation between damage mechanisms and fatigue life in order to develop an analytical method for predicting fatigue life using physical behaviour of the composites. In order to reach this objective first a literature study was performed, followed by fatigue tests. The data collected during the fatigue tests were then analysed, to investigate the relation between the damage mechanisms found and the cyclic work, strain energy release rate, dissipated energy and acoustic emission.

In chapter 2 a summary is given of the literature study performed for the thesis, providing background information for the tests and data analysis. In chapter 3 a description is given of the production of the test specimens, the fatigue test set-up and the approach to the data analysis performed. Then, in chapter 4 the results from the data analysis are presented and discussed using background information from chapter 2, other literature found during the analysis and observations during the fatigue tests. Lastly, in chapter 5 the conclusions during the thesis are summarised and a list of recommendations is given.

2

Background

2.1. Damage Mechanisms

There is a difference in how damage evolves between quasi-static loading and cyclic loading. This is due to the difference in rate and level at which the loading is applied.

With quasi-static loading the damage starts to develop after the first fibre breaks, which depends on the defect size distribution in the fibres. The damage mechanisms are crack propagation in the matrix, matrix yielding and de-bonding at the fibre-matrix interface. The damage mechanism that occurs after the fibre breakage depends on the material properties of the fibres, matrix and the fibre-matrix interface [40].

With cyclic loading the damage mechanisms depend on the applied stress levels. When the applied stress is higher than the tensile strength of the unidirectional (UD) ply, the damage mechanisms are similar to quasi-static loading. For a high stress level where the applied stress is higher than the tensile strength of the weakest fibre but lower than the overall composite strength, fibres will break randomly during the first load cycle. In the following load cycles the damage at the fibre breaks will evolve into debond cracks at the interface. The debond cracks can also evolve into transverse matrix cracks. For medium stress levels between the weakest fibre strength and the fatigue limit, matrix cracking occurs as a damage mechanism. When the stress level is below the fatigue limit, the fatigue life may be infinite when the defects are too small to propagate or the arresting mechanisms are high enough to prevent propagation [40].
The difference in damage mechanisms causes the difference in energy dissipation per area between quasi-static and cyclic loading [1].

Damage accumulates in three different stages. In the first stage during the first few cycles damage increases rapidly, due to the different damage modes present. In the second stage damage increases slowly and during the last stage at the end of fatigue life damage increases rapidly again due to fibre fracture [26]. Damage accumulation can be characterized using damage parameter D. D can be determined by the remaining stiffness or applied cycles, and has a range from 0 to 1. A composite is undamaged when $D = 0$ and has failed when $D = 1$. This parameter is used for residual strength and cohesive zone models.

Pipes et al [38] discovered that a crack at a notch propagates in the loading direction and that material properties are changed locally around the hole. The hole also caused a strain concentration factor at the hole edge with a large strain gradient.
In a quasi-isotropic glass fibre reinforced polymer (GFRP) damage initiates first in the 90° plies with matrix cracking at the hole boundary. This is followed by matrix cracking of the ±45° plies. Then splitting occurs in the 0° plies and local delaminations at the interfaces between the 45° and 90° plies. Final failure will consist of fibre fracture and fibre pull-out. The fracture path of the failed fibres in the 0° plies was found to be on the centre-line of the hole [8].
Broughton et al[8] also noted that the damage zone of the notched quasi-isotropic GFRP developed similarly to the quasi-isotropic carbon fibre reinforced polymer (CFRP) described by Green et al [21].
Green et al [21] described that there are two different types of regions of delaminations, as shown in figure 2.1. The inner delamination regions are at the hole boundary and are enclosed by 45° and -45° matrix cracks from the centreline. The outer delamination region starts after the 45° and -45° matrix cracks crossed each other and continues to the edges of the specimen. The delamination regions are split up by 90° matrix cracks. The size of the local delaminations in these regions has a similar magnitude as the ply thickness.

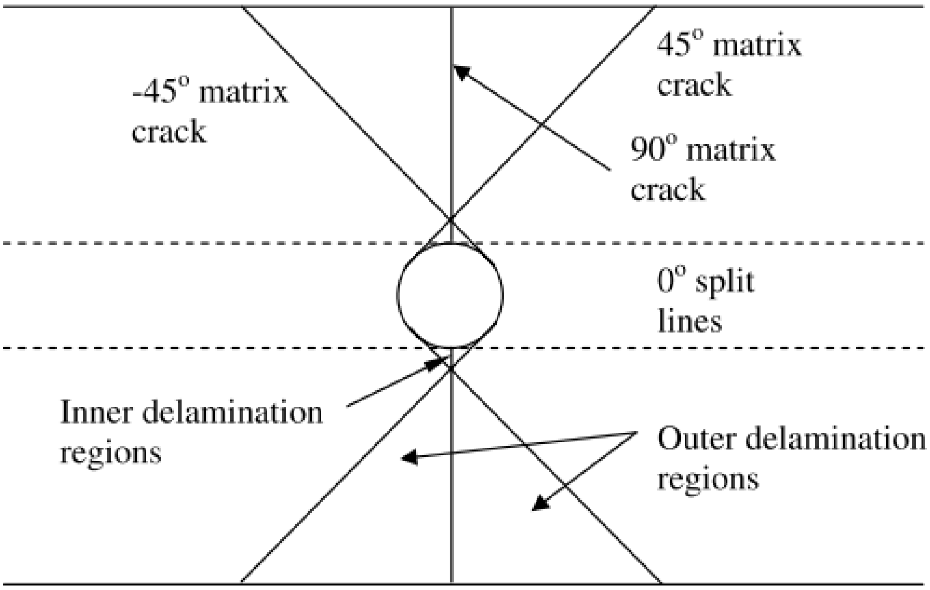

Figure 2.1: Damage zones in a notched quasi-isotropic composite. Retrieved from [21]

The damage develops in four different stages. The first stage of damage will be the isolated damage mechanisms described before. During the second stage the isolated damages will join together into extensive damage in the inner delamination regions. Then during the third stage the damage propagates from the hole edge to the specimen's edge through the outer delamination regions. At the last stage matrix cracking and delaminations occur away from the hole [21].

Therefore, in order to characterize each damage mechanism separately, the damage mechanisms have to remain isolated during the fatigue test. The 0° split lines can be characterised by testing coupons with a 0° lay-up, while the 90° matrix cracks can be characterised by testing coupons with a 0 °/90° lay-up. By testing coupons with a ±45° lay-up the matrix cracks and delaminations in the 45° and -45° plies can be characterised. During these tests the interaction between the delaminations in the ±45° plies and the 90° matrix cracks will however not be present. This has to be taken into account when comparing the individual results with a quasi-isotropic coupon.

Delaminations can be seen in a load-displacement diagram as a drop in load. The amount of load drops depends on hole size and give an indication on how the delamination propagates [21]. The dominant failure mechanism also depends on hole size, as the hole size increases the failure mechanism changes from delamination to fibre pull-out to brittle failure. When the failure mechanism is fibre pull-out the fracture surface is rough, while the fracture surface of brittle failure is smooth [21].

2.2. Fatigue Life Assessment and Prediction

2.2.1. Tests

The standardized tests for fibre-reinforced polymers (FRP) for different delamination modes under quasi-static loading can be found in table 2.1. These standard tests can be used to determine the fracture toughness or interlaminar delamination resistance for unidirectional (UD) composite plies [10]. These tests allow for reproducible results that can be used in models for predicting fatigue life.

Table 2.1: Available Standard tests for fibre-reinforced polymers under quasi-static loading for different delamination modes

Delamination mode	Test
Mode I	ASTM D5528 JIS K7086 ISO 15024
Mode II	JIS K7086
Mode I/II	ASTM D6671

For FRP under cyclic loading there is currently only a standard test method for mode I tension-tension delamination onset (ASTM D6115), but standard tests for other delamination modes are currently under development [11].

There are no specified standards for testing open-hole specimens in fatigue, however the test geometry and loading specified by ASTM D5766 [4], which is used for open-hole tensile strength testing, can be used for open-hole tension-tension fatigue testing [8].

Non-destructive testing techniques that can be used for monitoring damage development during fatigue are: acoustic emission, ultrasonic testing, optical and scanning electronic microscopy, pulse thermography and X-ray computed thermography. Optical and scanning electronic microscopy are however limited to monitoring damage development on the surface, but can be used to characterise the fracture surfaces after failure. For pulse thermography the depth of penetration is limited by the amount of heat that the system can emit [8]. X-ray computed thermography is capable of 3D mapping the damage developed in the laminate, but requires radioactive material [33]. Acoustic emission is capable of identifying micro-cracking and the wave forms can be used to distinguish between damage mechanisms [3]. Ultrasonic testing is capable of mapping crack propagation, but only after pausing the test. Visual detection using cameras such as Digital Image Correlation can be used to monitor the crack length [3, 36], however as Amaral et al [3] noted the entire crack will not be visible on the surface so an effective crack length should be used.

2.2.2. Models

For predicting fatigue life in composites there are models based on different concepts: fracture mechanics, cohesive zone modelling and residual strength. For notches, specifically, the theory of critical distances can also be applied.

Fracture mechanics

Fracture mechanics is used to characterize fracture toughness or delamination resistance under applied loads, stresses or deformations. Delamination propagation is described using the strain energy release rate (SERR). The SERR is determined analytically, with finite element analysis or with experimental data [35]. For quasi-static loading there are standard test methods for modes I, II and fixed ratio mixed mode I/II [10]. The delamination rate is then determined as a function of the SERR with the Paris relation as given by

$$\frac{da}{dN} = Cf(G)^m \tag{2.1}$$

where the constants C and m have to determined by curve fitting experimental data, which means that these constants are phenomenological and lack physical meaning. There is still discussion about what similitude parameter should be used for this equation. [35] The lack of physical explanation in these models means that they are unable to explain the crack growth behaviour in composites and are only able to predict the crack propagation. Therefore, Yao et al [52] recommended that a prediction model for delamination based on energy balance should be made.

Amaral et al[1] proposed the use of an average SERR, G^*, as a similitude parameter, which describes the energy released through crack growth. The energy required per crack extension depends on the damage mechanisms present at the fracture surface. Less energy is dissipated per crack extension when the fracture surface is smoother or there are less damage features present at the fracture surface. The damage mechanisms depend on the crack growth rate.

Finite Element Models

Delamination within composites can also be predicted using finite element models. Two different techniques can be used to predict the onset and crack growth: Virtual Crack Closure Technique (VCCT) and Cohesive Zone Modelling (CZM). CZM does not require a pre-existing crack for predicting the onset and growth of a crack and does not require that the mesh is redefined during simulation, while VCCT does. This is why CZM is preferred over VCCT to predict delamination onset and fatigue life for undamaged composite laminates.
CZM uses cohesive zone elements at the interfaces where delamination may occur. The fracture toughness in these elements are defined by a given traction-separation law. This law depends on the material properties and behaviour, and describes the shear stresses at the crack tip due to crack opening for modes I and II. The traction-separation law can be constant, linear or quasi-exponential softening. The models can be used for Mode I [16, 19, 20, 29, 39, 50], Mode II [19, 20, 39, 50], Mode III [18, 19, 39] and Mixed Mode [17, 31]. A fine discretization along the crack path is required for convergence and to properly capture the non-linear processes in the process zone. The damage growth in the element is simulated using a damage parameter, which represents the stiffness degradation in an element due to the damage. The cracked material is assumed to be stress free and the failure process zone is assumed to be lumped in the crack plane. The length where the cohesive zone is defined and where a finer mesh should be applied is defined as the cohesive zone length [44]. The cohesive zone length depends on the characteristic length, cohesive law shape and structure size for a given fracture mode [44].

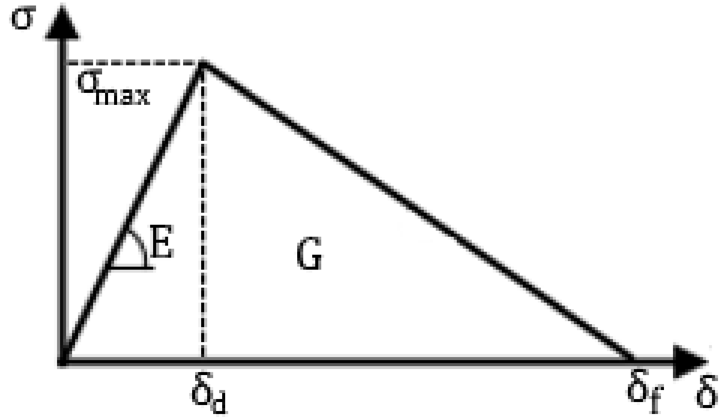

Figure 2.2: A bi-linear traction-separation law that is used in cohesive zone elements. Delamination starts in the element when the displacement has reached δ_d and the element has failed when the displacement has reached δ_f.

The cohesive zone model developed by Nixon-Pearson et al [34] is capable of predicting the damage sequence and overall slope of the fatigue life curve. The cohesive elements follow a bi-linear traction separation law as shown in figure 2.2, where the stress initially increases with the displacement with the stiffness until fibre failure occurs at δ_d, after which the stress decreases again with increasing displacement until final failure at δ_f. The bi-linear traction-separation law used for mixed mode is a combination of the constitutive laws for mode I and mode II [34]. This means that the values used for fracture toughness G, stiffness E and maximum stress σ_{max} are in the range of values for mode I and mode II delamination.

Residual Strength

Models based on residual strength reduce the strength or stiffness of the laminate after each cycle or block of loading, as the performance of the laminate decreases due to damage accumulating during a cycle. The degradation depends on the severity of the cyclic loading, scatter and number of cycles and can be used to evaluate the damage progress using the damage parameter D. The predictions are statistical and phenomenological and most models cannot be used universally [37]. The models are based on the cumulative probability of failure per cycle. Kassapoglou et al [25] found that when taking the damage propagation into account this probability will vary for each cycle, while models that do not take damage into account will have a constant probability, assuming that both the static strength and residual strength follow a two-parameter Weibull distribution. Local stress distribution has to be analysed after each cycle in case local failure requires an adjustment of global residual strength. The reduction in residual strength can be associated with different damage mechanisms, but the magnitude of reduction in residual strength can not be correlated with a single type of damage [25]. In some models it is assumed that the residual strength follows a power law in order to include the large drop in strength at the end of life [15].

The models proposed by Vinayak et al[43, 51] predict the fatigue life using an analysis of the stresses, the residual strength and failure criteria of an open-hole laminate for uni-axial and multi-axial random loading. For the failure analysis a modified fibre failure criterion is used. The criterion is modified to use fatigue residual strength instead of unnotched static strength. The number of cycles for each applied stress level during the random loading is determined with the rainflow counting technique. Determining the residual strength after a number of cycles N is done iteratively. The number of cycles to failure is then determined by the number of cycles required for the residual strength to go below the applied stress level. The method for these models requires experimental S-N curves for tension-tension and compression-compression, loading history and detailed information of the laminate, so the models are quite complex. However, according to Philippidis and Passipoularidis [37] the simpler models for residual strength are more effective, due to the large amount of data required for more complicated models, that has to be retrieved from multiple tests under the same conditions. Philippidis and Passipoularidis also found that the simplest model, a linear model by Broutman and Sahu [9], was the only model that could be safely applied universally.

Theory of critical distances

The theory of critical distances can be applied to any material with a circular hole [47]. It is hypothetically capable of predicting the fracture toughness during static and fatigue loading as the crack propagates [48]. The theory uses a length scale L given by

$$L = \frac{1}{\pi}\left(\frac{K_c}{\sigma_u}\right)^2 \tag{2.2}$$

where for blunt notches L gives the critical notch radius at which a transition occurs from the hole's K_t having no effect on the strength to having an effect on the strength [47].

K_c is the fracture toughness of the material and can be replaced by the crack propagation threshold ΔK_{th} for fatigue loading. The tensile strength of the material σ_u can be replaced by the fatigue limit $\Delta\sigma_o$. There are four methods that use the theory of critical distances to predict the fracture toughness and fatigue limit. The point method uses an elastic stress analysis to determine the stress at a distance of $L/2$. It is assumed that failure occurs when the stress exceeds the appropriate cyclic stress. For circular holes the failure stress is given by [48]

$$\sigma_f = \frac{\sigma_u}{\left(1 + \frac{1}{2}\left(\frac{a}{a+L/2}\right)^2 + \frac{3}{2}\left(\frac{a}{a+L/2}\right)^4\right)} \tag{2.3}$$

in which a represents the crack length. With the line method the stress is the average stress along a line with length 2L starting from the notch root. The imaginary crack method places an imaginary crack at the notch root and the material will fail when the crack reaches the fatigue threshold ΔK_{th}. The length of this imaginary crack is L. The fourth method is finite fracture mechanics assumes a finite amount of crack extension. The crack extension will be 2L. These four methods give similar results depending on the geometry of the cracks and notches [47].

2.3. Energy Dissipation

2.3.1. Composites

In composites the energy dissipated is contributed to micro-cracks in the process zone near the crack tip. The size of the process zone depends on the stress distribution [3]. Belaadi et al [6] observed hysteresis loops in a load-displacement diagram during cyclic loading and determined the energy dissipated per volume by calculating the area of the hysteresis loop. Therefore, the dissipated strain energy can be determined by measuring the loads and displacements during each cycle and calculating the area in the hysteresis loop. When calculating the strain energy, a correction has to be applied to take into account non-linearity in the load-displacement diagram due to compliance of the test fixture [2]. Inaccuracies in displacement measurements can also be reduced by using an external extensometer for measuring the displacements. To prevent energy dissipation due to heat, the frequency of the fatigue test has to be low. The acoustic energy dissipated can be measured through acoustic emission similarly to metals. The data from the acoustic emission measurements can also be used to monitor damage accumulation [3] and damage mechanisms are identifiable by their peak frequencies [22]. Therefore, acoustic emission can also be used to monitor the damage mechanisms as described in chapter 2.1. It is still unclear whether the amount of dissipated mechanical energy is unique for each fracture mode, as well.

It was also noted that the energy dissipated per volume as a function of the number of cycles depended strongly on the stress ratio, which is most notable for low number of cycles, where the energy dissipated increases with stress ratio. Amaral et al [3] also observed that for high stress ratios the resistance to crack growth changes after 6000 cycles, while this change is minimal or absent for low stress ratios. Thus, the change in resistance to crack growth can be related to an increase in dissipated energy. Thus, a method for constructing fatigue master curves using a relation based on energy dissipation with a low stress ratio may not be applicable for a constructing fatigue master curve with a high stress ratio after 6000 cycles. Therefore, in order to create a model, fatigue tests should be performed at low and high stress ratios.

Mohavedi-Rad et al [30] found that the amount of energy dissipated depends on the number of cycles and fatigue stress levels, due to friction caused by damage growth. The relation between the increase in dissipated energy and number of cycles until failure appeared to be nearly linear when presented on a double logarithmic scale as shown in figure 2.3. This suggests that there is relation between the fatigue life curve and the total amount of dissipated energy during the fatigue life. So, in order to be able to relate the fatigue life to the damage mechanisms using energy dissipation, the energy dissipation at different stress levels should be measured and a S-N curve should be constructed. Whether the total amount of energy dissipated also depends on the fracture modes still has to be investigated. If the total dissipated energy is found to be dependent on both the fatigue life and fracture modes, then fatigue life could be predicted based on possible fracture modes and energy dissipation.

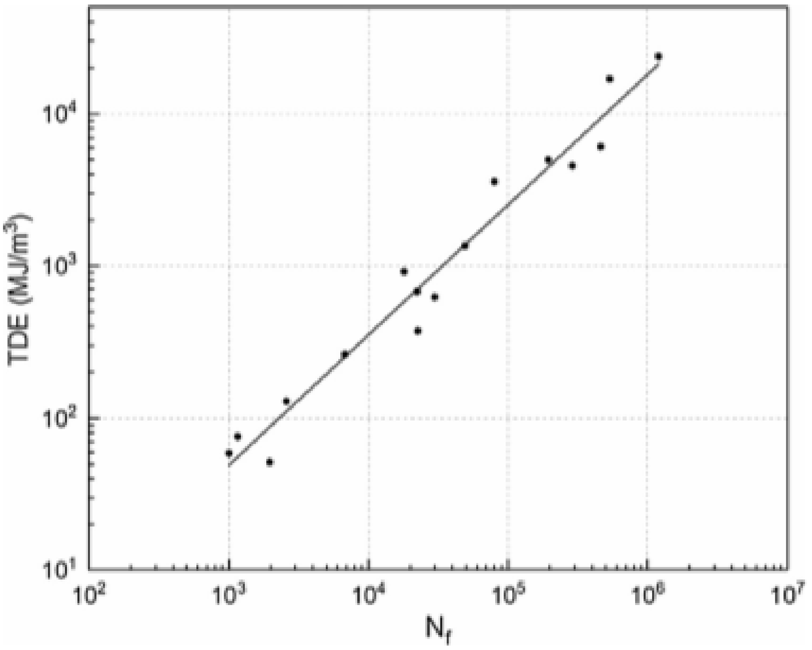

Figure 2.3: Total dissipated energy (TDE) versus the number of cycles to failure (N_f) on a double logarithmic scale. Retrieved from [30].

2.3.2. Adhesive bonds

Pascoe et al [36] observed that when plotting the crack growth rate against the dissipated energy per cycle there is only a small dependency on the stress ratio.A power law can be used to describe the correlation between the crack growth rate and energy dissipated per cycle. However, with this relation there was one outlier which was not explained. The strain energy for each was determined using the load and displacement of the specimen. The data points were curve fitted using a power law and the derivative was used for the dissipated energy per cycle.

3

Test Methods

3.1. Production

The coupons used were laminates made with HexPly 8552 prepreg tape [14]. The lay-ups used were $[0]_{24}$, $[(0/90)_6]_s$, $[(45/-45)_6]_s$ and $[(0/90/45/-45)_3]_s$. First, large composite plates were manufactured using hand lay-up, by building two halves of twelve layers each and then placing one half on top of the other. The laminates were debulked after each layer was placed. Then, the laminate was cured in an autoclave according to manufacturer specifications. Before placing the vacuum bag, an aluminium plate was placed on top of the uncured laminate to ensure a smooth surface on both sides. The dimensions of the plates are given in table 3.1. The width and length were measured using measuring tape; the thickness of the plates was measured using a thickness gauge at three different points of the plate and taking the average.

Table 3.1: Composite plate dimensions after they were removed from the autoclave. The thickness was measured using a thickness gauge. The width and length were measured using a measuring tape.

ID	Lay-up	Thickness [mm]	Width [mm]	Length [mm]
8552-024-14-03	$[0]_{24}$	4.3	370	600
8552-0129012-17-04	$[(0/90)_6]_s$	4.2	600	1050
8552-QI-16-04	$[(0/90/45/-45)_3]_s$	4.4	450	600

Then, the plates were scanned using a C-scan to check for possible defects, so their locations are known before machining the plates into coupons. The angle-ply coupons were machined by first cutting part of the plate 8552-0129012-17-04 under a 45 degree angle, after which the coupons were machined. This was done to save time with hand lay-up. Afterwards the coupons are machined according to the geometry as shown in figure 3.1 based on the requirements from ASTMD5766 standard for tensile testing open hole composite coupons [4], as the geometry is also suitable for tension-tension fatigue testing [21].

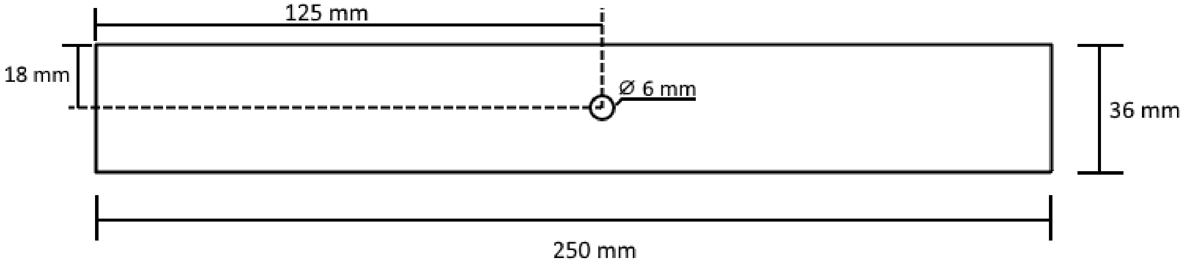

Figure 3.1: Specimen dimensions which were used for machining

The average dimensions including thickness of each batch of coupons are given in table 3.2 and were all measured with the same caliper. The length of the coupons were measured using a measuring tape. Before each test the coupons were also painted with a random speckle pattern in the area around the hole, as this is area of interest for the digital cameras.

Table 3.2: Average dimension for each coupon lay-up. The width, thickness and diameter were all measured using the same caliper. The length of each coupon was measured using the same measuring tape.

Lay-up	Width [mm]	Length [mm]	Thickness [mm]	Diameter [mm]
$[0]_{24}$	36.07	250	4.34	6.35
$[(45/-45)_6]_s$	36.07	250	4.36	6.35
$[(0/90)_6]_s$	36.06	250	4.37	6.35
$[(0/90/45/-45)_3]_s$	36.08	250	4.37	6.35

3.2. Fatigue Tests

The fatigue tests were performed using a MTS 100 kN fatigue machine using clamps with smooth surfaces to clamp the specimen at both ends. All specimens were tested with frequency $f = 5Hz$, stress ratio $R = 0.1$ and constant amplitude fatigue load. The load levels at which each lay-up was tested is given in table 3.3. After each 100th load cycle, there was a segment were the coupon was held at maximum load for 0.5s after which it returned to the minimum load and continued with the load cycles, as shown in figure 3.2. The peak and valley loads and displacements were recorded by the test bench for each cycle. The load and displacement were recorded by the test bench during the segment after each 100th load cycle.

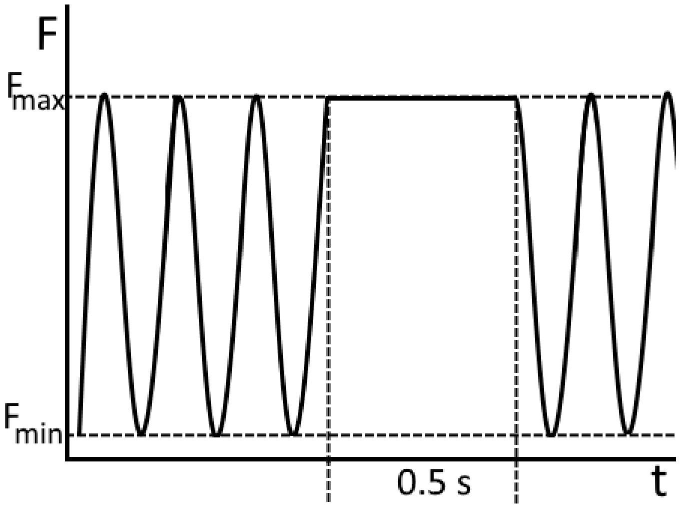

Figure 3.2: Sketch of load cycles over time

Table 3.3: Load levels used for each lay-up with their corresponding minimum and maximum load.

Lay-up	Load Level	Maximum Load [kN]	Minimum Load [kN]
$[0]_{24}$	Low	50	5.0
	Medium	53	5.3
	High	55	5.5
$[(45/-45)_6]_s$	Low	16	1.6
	Medium	18	1.8
	High	20	2.0
$[(0/90)_6]_s$	Low	60	6.0
	Medium	62	6.2
	High	64	6.4
$[(0/90/45/-45)_3]_s$	Low	52	5.2
	Medium	53	5.3

During the test the acoustic emission was measured to relate acoustic emission features to damage mechanisms and crack growth. For the acoustic emission measurements, two Vallen VS900-M broadband sensors [46] were clamped at either side of the coupon to accurately capture the damage growth around the open hole. Before the sensors were clamped to the specimen, a drop of coupling gel was applied to the sensors surface and spread by moving the sensor around on the specimen surface. The sensors were placed at least 30 mm away from the open hole for measurements.

The sensors were connected to a pre-amplifier with 34 dB gain and a 8 channel Amsy-6 system from Vallen Systeme. The Amsy-6 system was also connected to the test bench in order to record the bench load for each acoustic emission hit. The damage accumulation will be characterised by energy pulses measured by the acoustic emission sensors. Different damage modes can be distinguished based on their unique energy pulses. The load was measured alongside the acoustic emission measurements to couple the damage accumulation to the load cycles. The acoustic emission measurements were started before the fatigue test started and measurements stopped before the sensors were removed from the coupons. Acoustic emission hits were registered if the amplitude exceeded 50 dB.

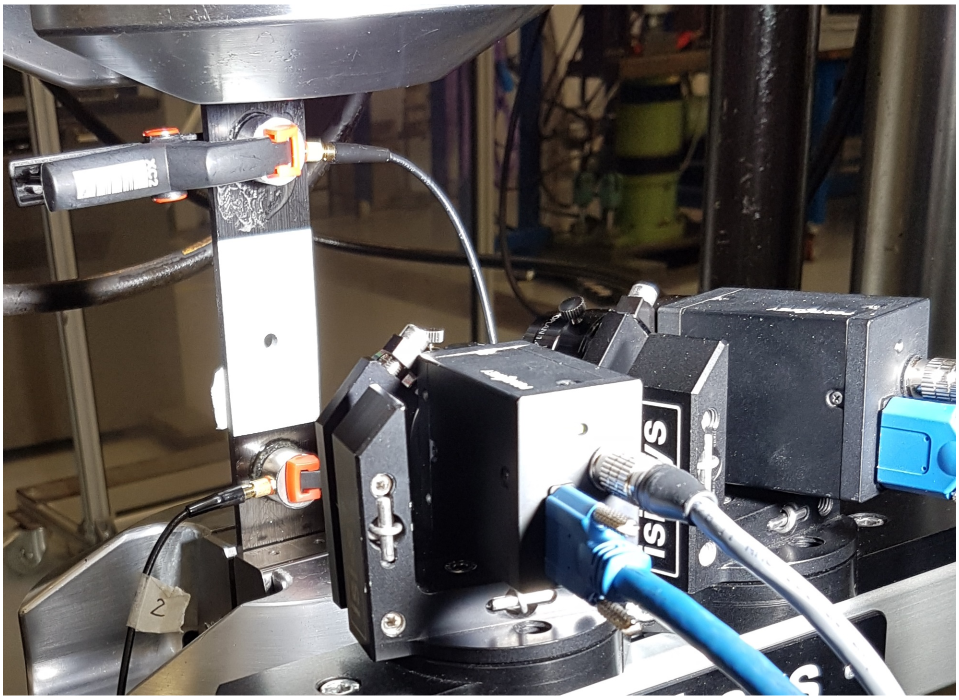

Figure 3.3: Picture of the test set-up. The upper acoustic emission sensor clamped to the specimen is for channel 1, while the bottom sensor is for channel 2.

Digital Image Correlation (DIC) was used to monitor crack growth and damage type. For the DIC, two cameras from isi-sys suitable for Vic-3D were set up such that the area of interest was fully in focus. Then, the camera set-up was calibrated and a picture was taken of each specimen before the start of the fatigue test to test the trigger signal for the cameras and to act as a reference picture for data processing.

Once the fatigue started a signal was given from the test bench to trigger the cameras at each 100th cycle and the pictures taken were stored on the PC the cameras were connected to.

3.3. Data Analysis

Three sets of data were collected during the tests: data from the test bench which contained the applied loads and displacement for each cycle, DIC photographs and acoustic emission measurements.

3.3.1. Load and Displacement

A Python script [45] was created to read the cyclic data retrieved from the test bench and determine the cyclic work done for each 100th cycle. This was done by finding the start and end index of each cycle and calculating the cyclic work using figure 3.4 and the following equation [35]:

$$U_{cyc} = \frac{1}{2}F_{max}(d_{max} - d_0) - \frac{1}{2}F_{min}(d_{min} - d_0) \tag{3.1}$$

with $d_0 = d_{min} - \frac{F_{min}}{k}$ and $k = \frac{F_{max} - F_{min}}{d_{max} - d_{min}}$, which are the displacement for when the load is zero and the slope of the load-displacement curve.

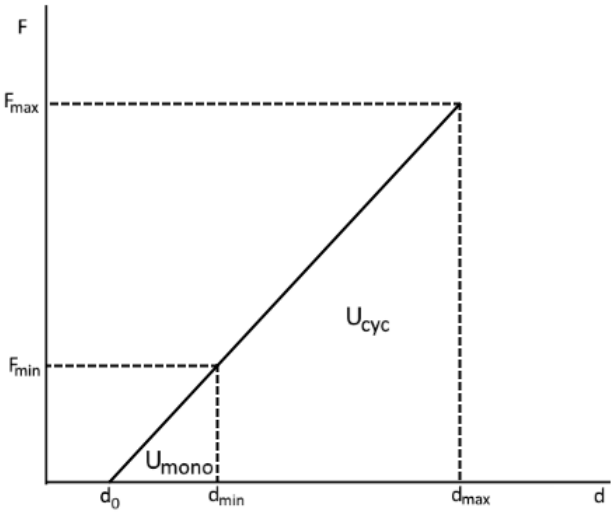

Figure 3.4: Sketch of the first half of a load cycle used to determine the cyclic work

The mechanical energy dissipated during each cycle was calculated by calculating the area of the hysteresis loop [6].This was done by using $U_d = U_1 - U_2$ where U_1 is the area underneath the load displacement curve of the first half of the load cycle, while U_2 is the area of the second half as shown in figure 3.5. The area was calculated using the data points recorded during each 100th load cycle and integrating them using the trapezoidal rule [13].

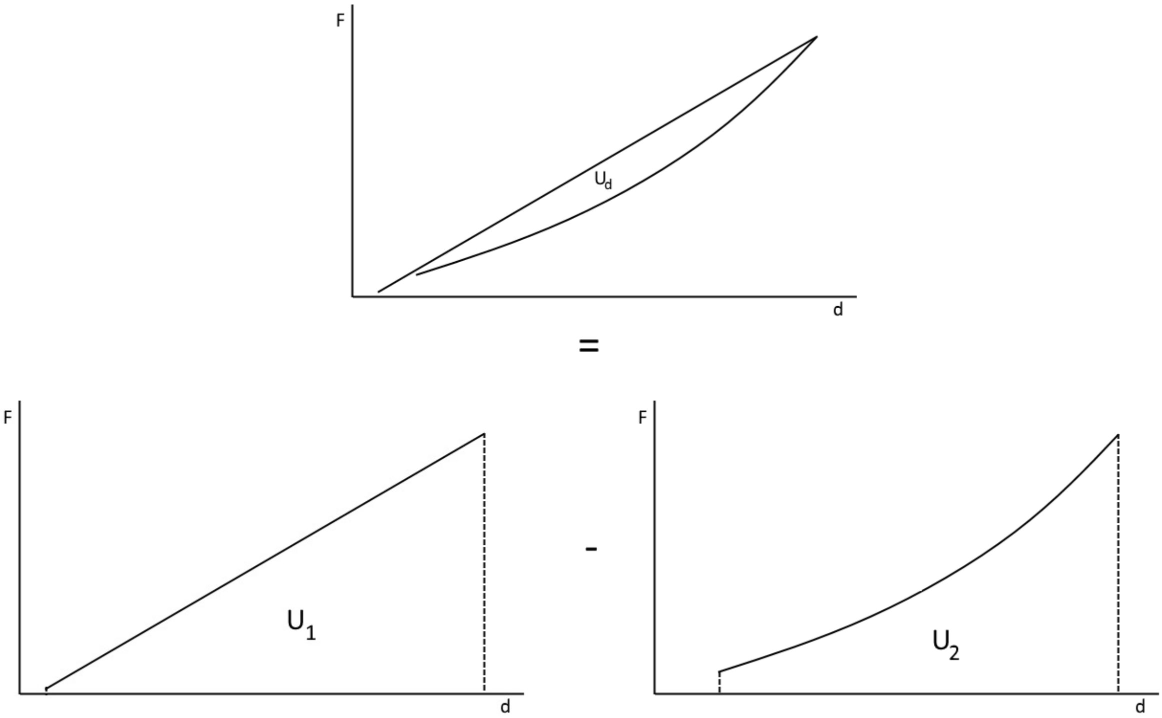

Figure 3.5: Sketch of the full load cycle used to determine the dissipated energy for each cycle.

It is expected that the dissipated energy will decrease over time, as the growth in damage should cause a decrease in stiffness, bringing the coupon stiffness during the first half of the load cycle closer to the stiffness during the second

half of the load cycle.
The cyclic work and dissipated energy for each cycle were then exported as a comma separated file and opened in Excel, where the data points were used to determine a trend-line.

3.3.2. DIC

The pictures taken by the DIC cameras were analysed using Vic3D, which determined the strain of the specimen in each picture using the first picture as reference. Then, the strain at which crack growth started was found by searching through the analysed pictures for the moment crack growth is apparent and determining the maximum strain around the crack. This strain was then used as a measure for crack growth.
For the $[0]_{24}$ and $[(0/90)_6]_s$ coupons, the crack length was determined by locating the crack tip and measuring the distance between the crack tip and the centre of the hole, as shown in figure 3.6.

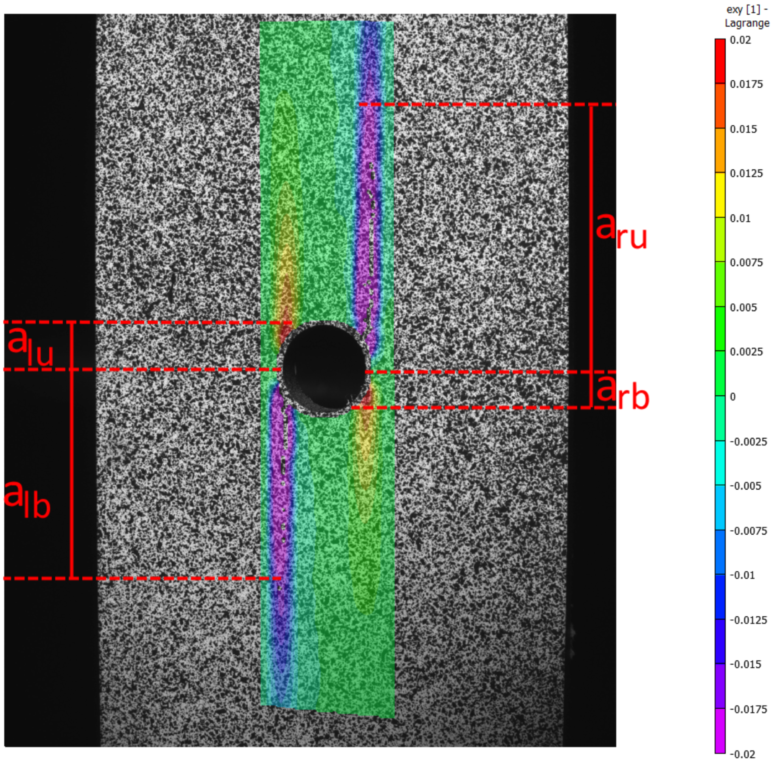

Figure 3.6: Determination of crack length for cracks in the 0° layer

The length of the damaged area for the 0° layer was then calculated as the average length of the left crack and the right crack as given by

$$a = \frac{a_{lu} + a_{lb} + a_{ru} + a_{rb}}{2} \tag{3.2}$$

The crack length in the 45° and -45° layers were measured along the 45° and -45° angles as shown in figures 3.7a and 3.7b.

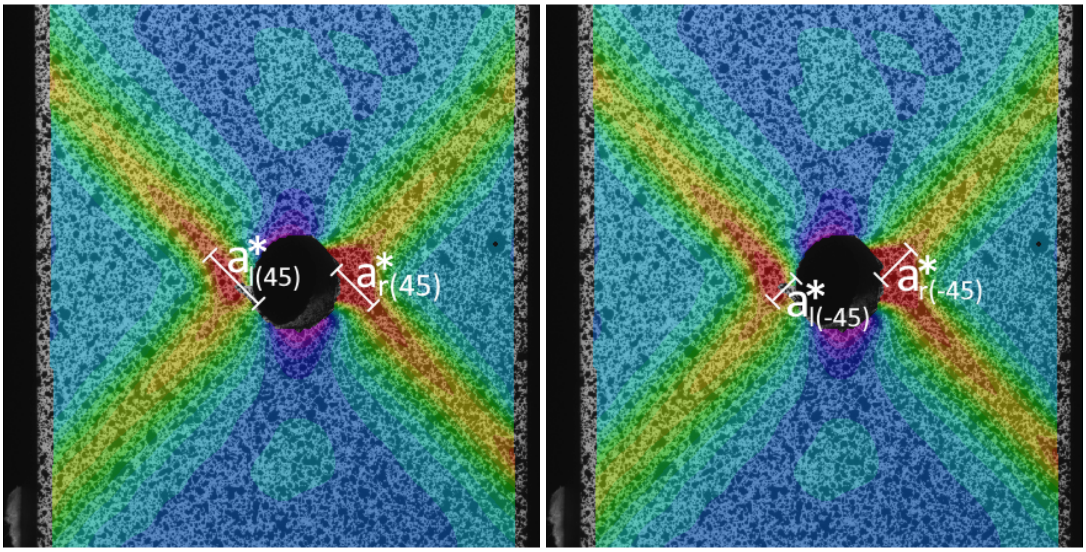

(a) Crack length in 45° direction with $a^*_{l(45)}$ for the crack on the left side of the hole and $a^*_{r(45)}$ on the right side of the hole.

(b) Crack length in -45° direction with $a^*_{l(-45)}$ for the crack on the left side of the hole and $a^*_{r(-45)}$ on the right side of the hole.

Figure 3.7: Determination of the crack length in the 45° and -45° directions indicated by a white line

For investigating the crack growth the total length of the cracks were taken in each direction, thus $a^*_{45} = a^*_{l(45)} + a^*_{r(45)}$ and $a^*_{-45} = a^*_{l(-45)} + a^*_{r(-45)}$. To determine the damaged area in the 45 and -45 layers, the crack lengths were projected along the vertical and horizontal axes with equations 3.3 and 3.4. This assumes that the two cracks at either side of the hole actually act as a singular crack. For the projection on the vertical axis first the length on each side of the hole was determined, after which the average of the two vertical lengths were taken as shown below:

$$\begin{aligned}
v_l &= a^*_{l(45)} \cos 45 + a^*_{l(-45)} \cos 45 = \frac{1}{2}\sqrt{2}a^*_{l(45)} + \frac{1}{2}\sqrt{2}a^*_{l(-45)} \\
v_r &= a^*_{r(45)} \cos 45 + a^*_{r(-45)} \cos 45 = \frac{1}{2}\sqrt{2}a^*_{r(45)} + \frac{1}{2}\sqrt{2}a^*_{r(-45)} \\
v &= \frac{v_l + v_r}{2} = \frac{1}{2}\left(\frac{1}{2}\sqrt{2}a^*_{l(45)} + \frac{1}{2}\sqrt{2}a^*_{l(-45)} + \frac{1}{2}\sqrt{2}a^*_{r(45)} + \frac{1}{2}\sqrt{2}a^*_{r(-45)}\right)
\end{aligned} \tag{3.3}$$

Because the projection starts from the centre-line the diameter of the hole does not have to be included in the vertical length of the damaged area.

For the projection on the horizontal axis, first the average length on each side of the hole was determined. Then, the sum of the two horizontal lengths were taken together with the diameter of the hole, as the open hole is part of the damaged area. This is shown below:

$$\begin{aligned}
h_l &= \frac{\frac{1}{2}\sqrt{2}a^*_{l(45)} + \frac{1}{2}\sqrt{2}a^*_{l(-45)}}{2} \\
h_r &= \frac{\frac{1}{2}\sqrt{2}a^*_{r(45)} + \frac{1}{2}\sqrt{2}a^*_{r(-45)}}{2} \\
h &= h_l + h_r + D
\end{aligned} \tag{3.4}$$

The data points were recorded and plotted in Excel and a trend-line was created going through the data points. The interval at which data points were taken depended on the amount of cycles that were tested. The derivative of the trend-lines were taken to determine da/dN.
Then, the displacement measured was plotted versus the crack length and the derivative of the trend-line was taken to calculate G with the equation below [23] assuming the load F is independent of the crack length a and displacement u dependent on a

$$G = \frac{F^2}{2b}\frac{dC}{da} = \frac{F^2}{2b}\frac{d(u/F)}{da} = \frac{F}{2b}\frac{du}{da} \tag{3.5}$$

Filling in equation 3.5 for maximum load and displacement, and minimum load and displacement will give $G_{max} = \frac{F_{max}}{2b}\frac{du_{max}}{da}$ and $G_{min} = \frac{F_{min}}{2b}\frac{du_{min}}{da}$, respectively. The similitude parameter used is $\Delta G = \left(\sqrt{G_{max}} - \sqrt{G_{min}}\right)^2$ [41].

To verify the measured displacement, the displacement was also calculated using the following equations for the coupons with unidirectional and crossply lay-ups:

$$\begin{aligned}
\sigma_1 &= \epsilon_1 E = \frac{u_1}{L-a}E \\
u_1 &= \frac{L-a}{E}\sigma_1 = \frac{L-a}{E}\frac{F}{wt} \\
\sigma_2 &= \epsilon_2 E = \frac{u_2}{a}E \\
u_2 &= \frac{a}{E}\sigma_2 = \frac{a}{E}\frac{F}{(w-D)t} \\
u &= u_1 + u_2 = \frac{F(L-a)}{Ewt} + \frac{Fa}{E(w-D)t}
\end{aligned} \tag{3.6}$$

For coupons with angleply lay-up the displacement was determined using $\Delta u = \frac{F(L-v)}{Ewt} + \frac{Fv}{E(w-h)t}$ with v and h as defined in equations (3.3) and (3.4).
The modulus of elasticity E was determined using thick laminate theory to calculate the ABD-matrix. Afterwards, the ABD-matrix in order to retrieve the abd-matrix. Then, the membrane stiffness $E = \frac{1}{a_{11}}$ was taken as the modulus of elasticity of the coupon.

3.3.3. Acoustic Emission

The acoustic emission data was first reduced by applying a filter with the following conditions:

- signal amplitude has to be at least 60 dB, as the damage mechanisms associated with AE hits below 60 dB are considered the least damaging [42];
- the signal rise time has to be at least 1 μs, as a rise time below 1 μs as a no physical meaning;
- the signal duration has to be less than 700 μs.

The features exported for each hit were: hit count, load in N, acoustic energy in eu, amplitude in dB, rise time in μs, duration in μs, time in hh:mm:ss and channel.
The cumulative acoustic energy and hit count for each sensor channel were also extracted in steps of 20 seconds. The time for each step was first converted to number of cycles, after which the mean energy and amount of hits between the two channels were taken to compare the increase of acoustic energy and hits with the observed trend in crack growth.

4

Results and Discussion

The results discussed in this chapter are based on the data made available at [45]. The data analysis steps were described in section 3.3.

4.1. DIC

The pictures for the DIC measurements were taken during the load segment as explained in section 3.2. The crack length measured for the different lay-ups are shown in figures 4.1 to 4.4. As shown in figure 3.6 the cracks in 0° direction started from the centre-line of the hole and grew in the direction of the loading. It can be seen in figures 4.1 and 4.2 that for the unidirectional and cross-ply lay-ups the crack in 0° direction increases steeply at the beginning and then levels off. This was expected as the effect of the stress concentration caused by the hole decreases when moving further away from the hole, decreasing the rate at which a crack grows.
The cracks in 45° and -45° direction in the angle-ply lay-ups slowly grows in the beginning and rapidly grows at the end of life, as shown in figure 4.3. The coupon starts to delaminate around the open hole after the cracks reached the edges of the coupon, which caused the sudden increase in crack length.
For the quasi-isotropic lay-up in figure 4.4 the cracks in 45° and -45° direction has a steep increase in length in the beginning and then levels off as the cracks reaches the ends of the coupon. Once the 45° and -45° cracks reached the ends of the coupon, the cracks in 0° started to increase faster in length.
The crack growth in the 90° layers could not be measured as the crack reached the edge of the coupon before the 100th cycle.

The damage modes found with DIC correspond with the damage mechanisms described in section 2.1, however no out-of-plane delamination was found in the QI coupons in the delamination regions as shown figure 2.1. Instead out-of-plane delaminations were found between the 0° split lines.

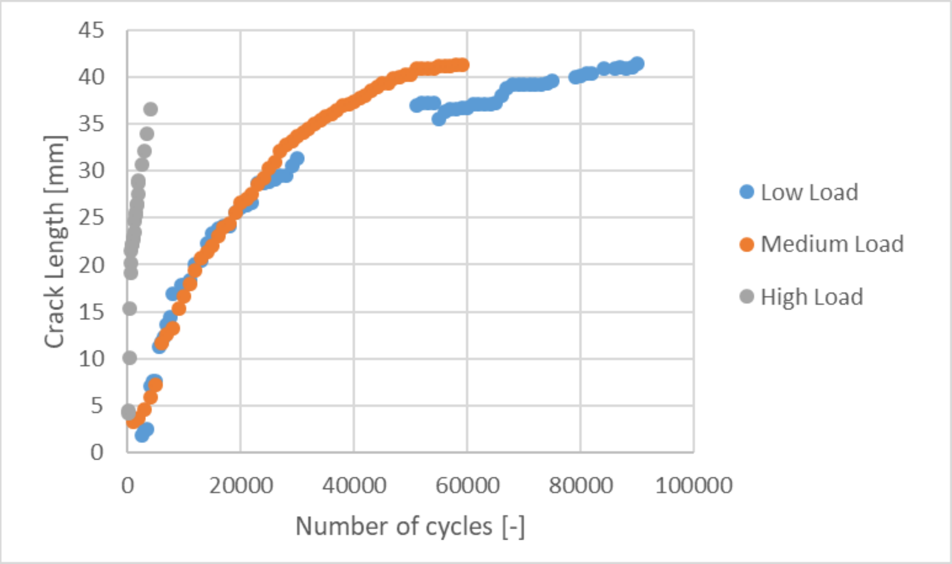

Figure 4.1: Crack length versus amount of load cycles for unidirectional coupons at tested load levels

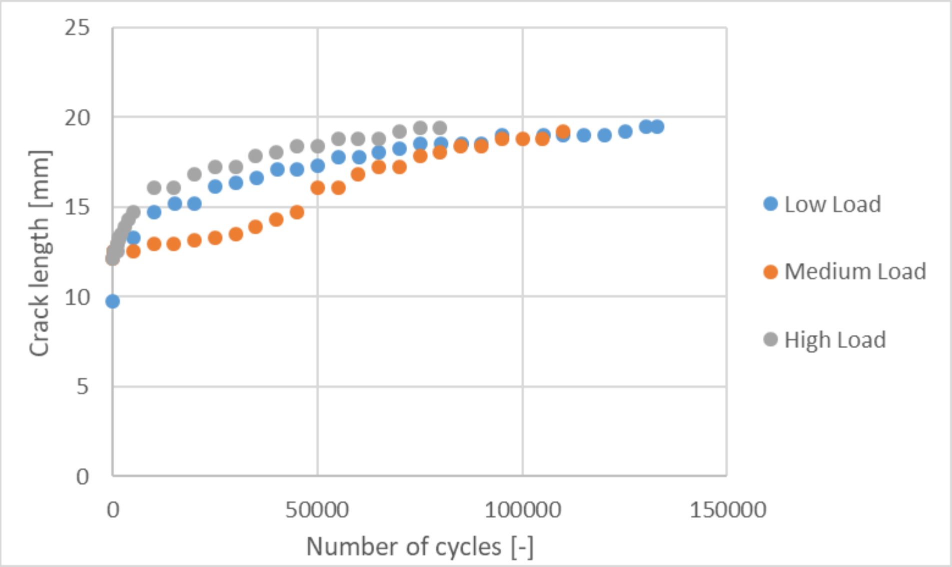

Figure 4.2: Crack length versus amount of load cycles for cross-ply coupons at tested load levels

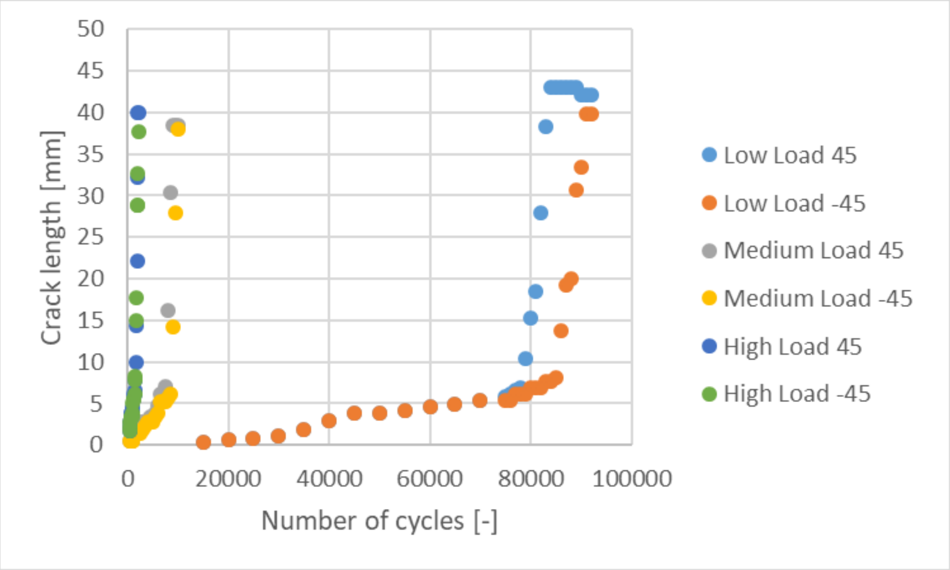

Figure 4.3: Crack length versus amount of load cycles for angle-ply coupons at tested load levels

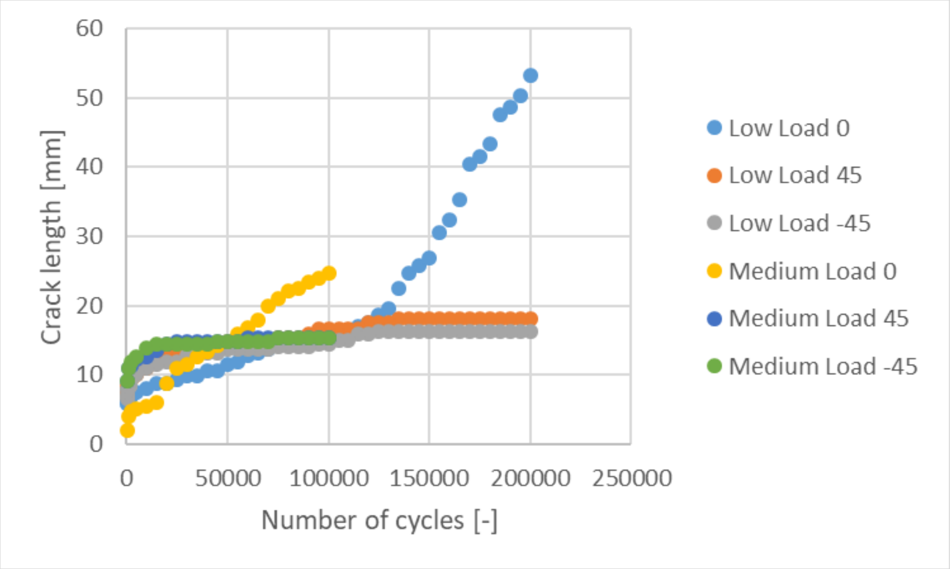

Figure 4.4: Crack length versus amount of load cycles for quasi-isotropic coupons at tested load levels

A power function was fitted as trend-line through the data points in order to determine the crack length as function of the number of cycles as shown in figures 4.5 to 4.8.It can be seen in figures 4.7 and 4.8 that a power curve does not accurately describe the entire crack growth. For the angle-ply coupons, the actual curve for the crack growth starts to deviate near end-of-life. This would mean that using the power curve to calculate da/dN will cause da/dN to be inaccurate for end-of-life. For the quasi-isotropic coupons the crack growth in the 0° plies deviate from a power curve. As said before, this was due to a delay in crack initiation after the matrix cracks in 45°/-45° plies started to progress. This deviation can affects the relation between crack growth rate and strain energy release rate.

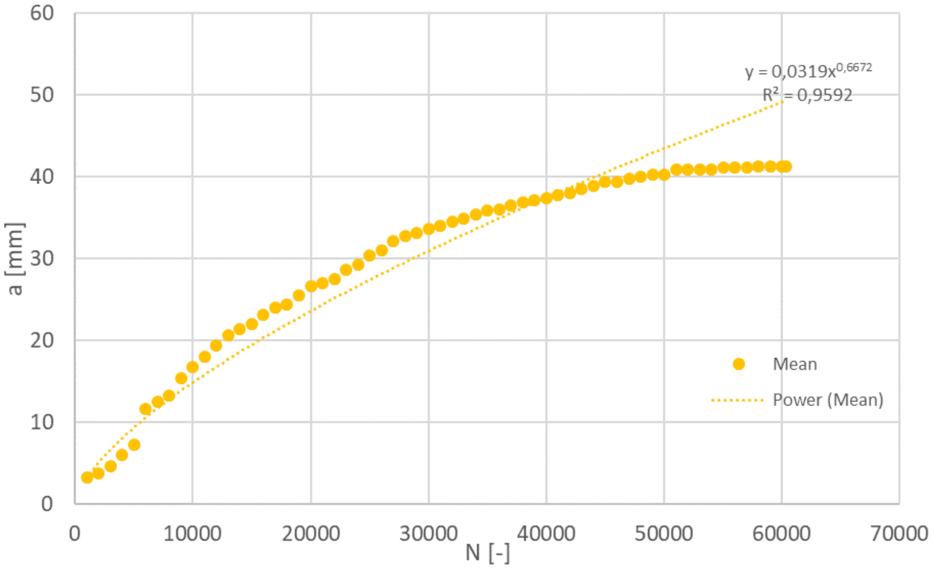

Figure 4.5: Crack length versus amount of load cycles with trend-line for unidirectional coupon tested at a maximum load of 53 kN

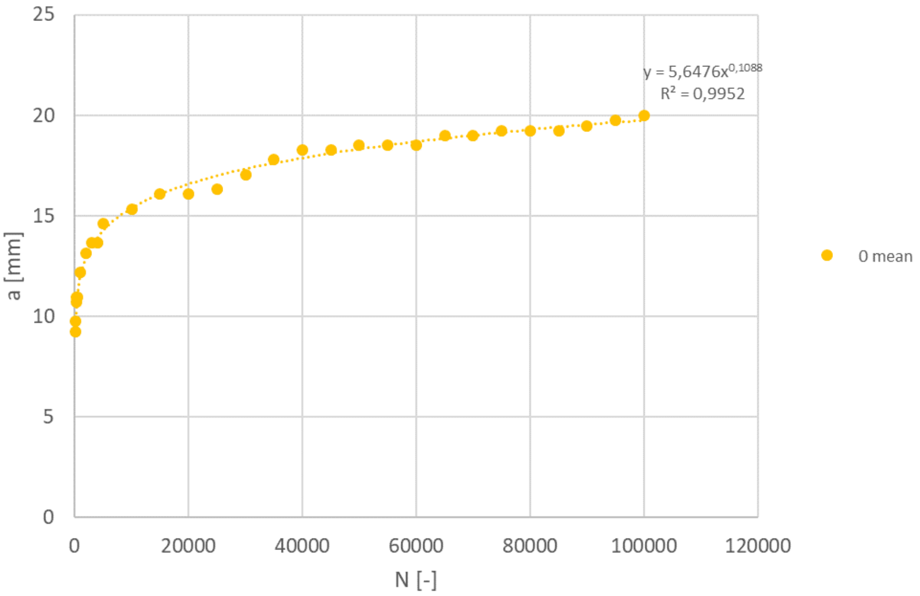

Figure 4.6: Crack length versus amount of load cycles with trend-line for cross-ply coupon tested at a maximum load of 62 kN

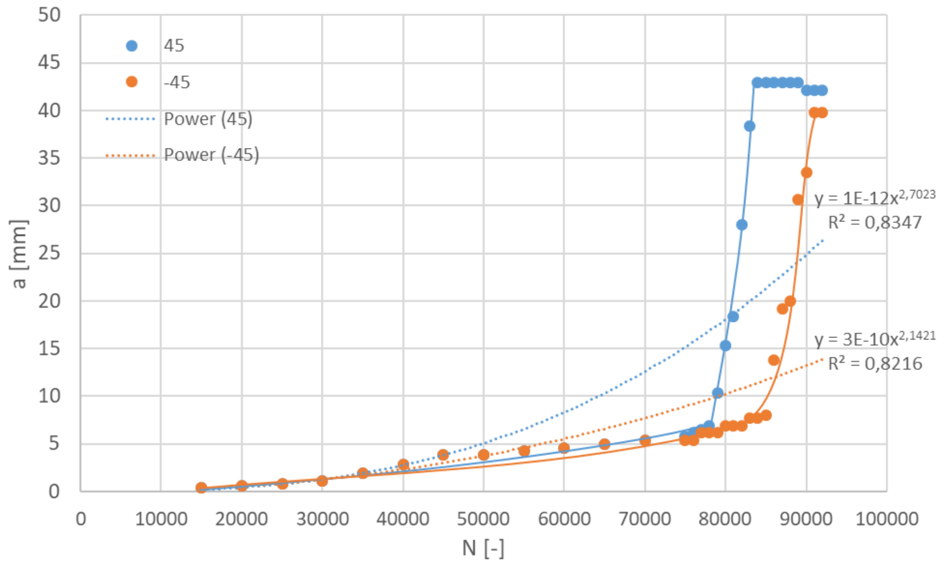

Figure 4.7: Crack length versus amount of load cycles with trend-lines for angle-ply coupon tested at a maximum load of 16 kN

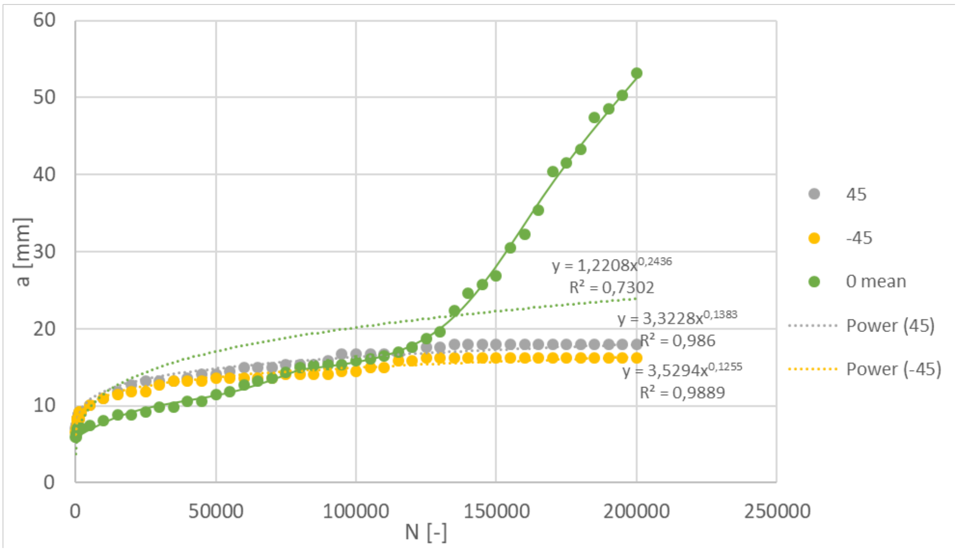

Figure 4.8: Crack length versus amount of load cycles with trend-lines for quasi-isotropic coupon tested at a maximum load of 52 kN

Because not all coupons were tested until full failure, it was decided to test until the cracks reached the edges of the coupon for ±45° cracks or until the cracks reached the edge of the DIC area. This resulted in the following fatigue curves shown in figure 4.9. The test results were also filled in the test matrix in table 4.1. It can be seen that the cross-ply and quasi-isotropic were tested at higher loads, but still had longer lives which was unexpected. This could be because of the stacking sequences used for cross-ply and quasi-isotropic influencing crack initiation and growth, and the definition used for failure.

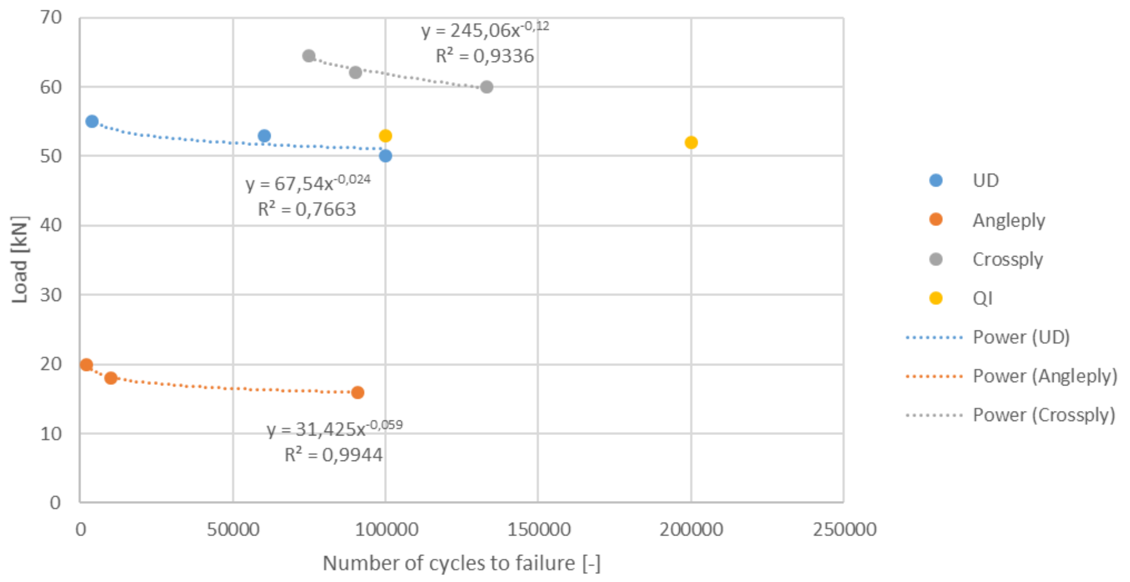

Figure 4.9: Fatigue curves for the various lay-ups unidirectional (UD), angle-ply, cross-ply and quasi-isotropic (QI). Failure was considered when the cracks measured had reached a defined length.

Table 4.1: Test matrix including lay-up of the coupons, load level, stress ratio, number of cycles until failure, maximum load and damage types found. Failure was considered when the cracks measured had reached a defined length.

Lay-up	Load level	Stress ratio	Number of cycles	Maximum load [kN]	Damage type
$[0]_{24}$	Low	0.1	100099	50	Fibre Splitting
	Medium	0.1	60299	53	
	High	0.1	3999	55	
$[(0/90)_6]_s$	Low	0.1	132999	60	Fibre Splitting Matrix Cracking
	Medium	0.1	89999	62	
	High	0.1	74999	64.5	
$[(45/-45)_6]_s$	Low	0.1	90999	16	Matrix Cracking Delamination
	Medium	0.1	9999	18	
	High	0.1	2199	20	
$[(0/90/45/-45)_3]_s$	Low	0.1	199999	52	Fibre Splitting Matrix Cracking Delamination
	Medium	0.1	99999	53	

4.2. Load Displacement data

Before calculating the cyclic work for each coupon, it was first checked whether a hysteresis loop was present in the load-displacement diagrams for each lay-up. This was done for three different cycles throughout a specimens life.

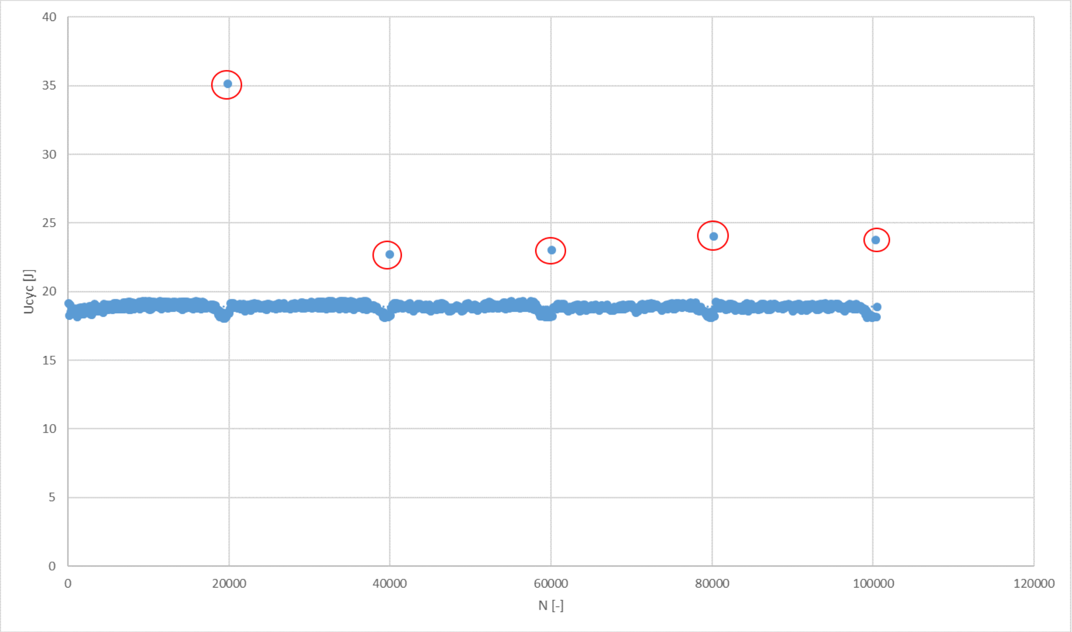

Figure 4.10: Cyclic work versus amount of cycles with outliers highlighted by a red circle

The data points highlighted in figure 4.10 were investigated by looking at the cyclic data from the test bench. It was found that these points corresponded with cycles were the first half of the cycle was 0.5s segment at which the coupon was held at maximum load and the second half of the cycle was the unloading of the coupon as described in section 3.2. Since this is not the type of load cycle under investigation, these points were treated as outliers and removed from the graph for determining the trend-line. This resulted in the graphs shown in figures 4.11 to 4.14.

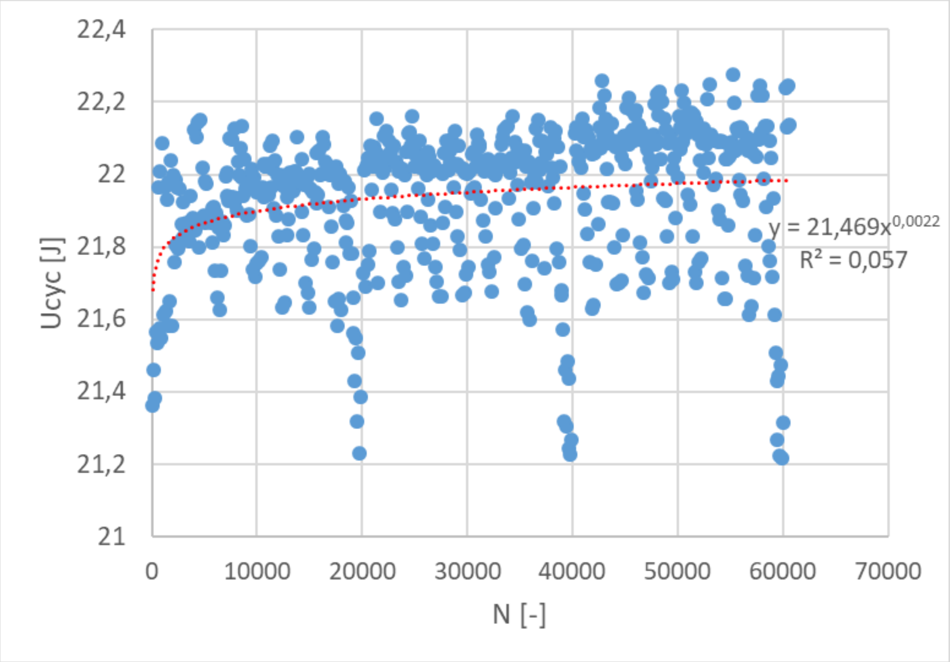

Figure 4.11: Cyclic work versus amount of cycles for unidirectional coupons tested with a maximum load of 53 kN

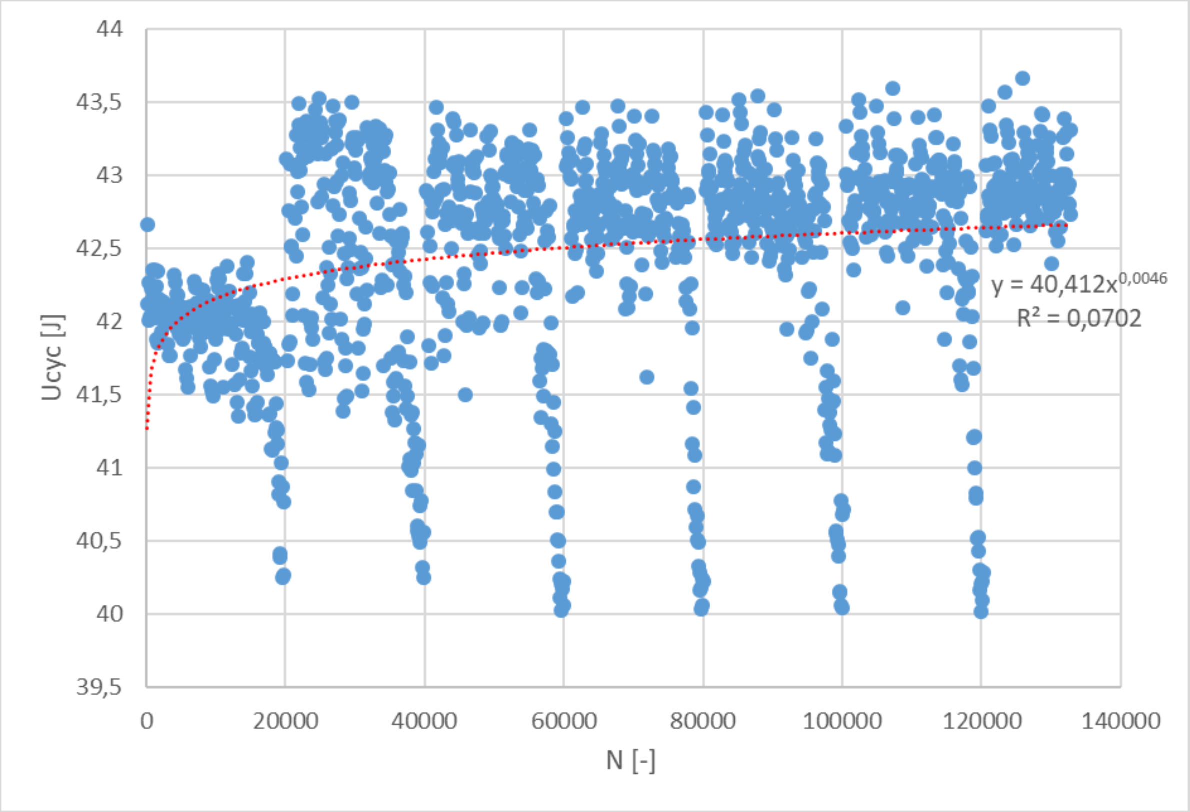

Figure 4.12: Cyclic work versus amount of cycles for cross-ply coupons tested with a maximum load of 60 kN

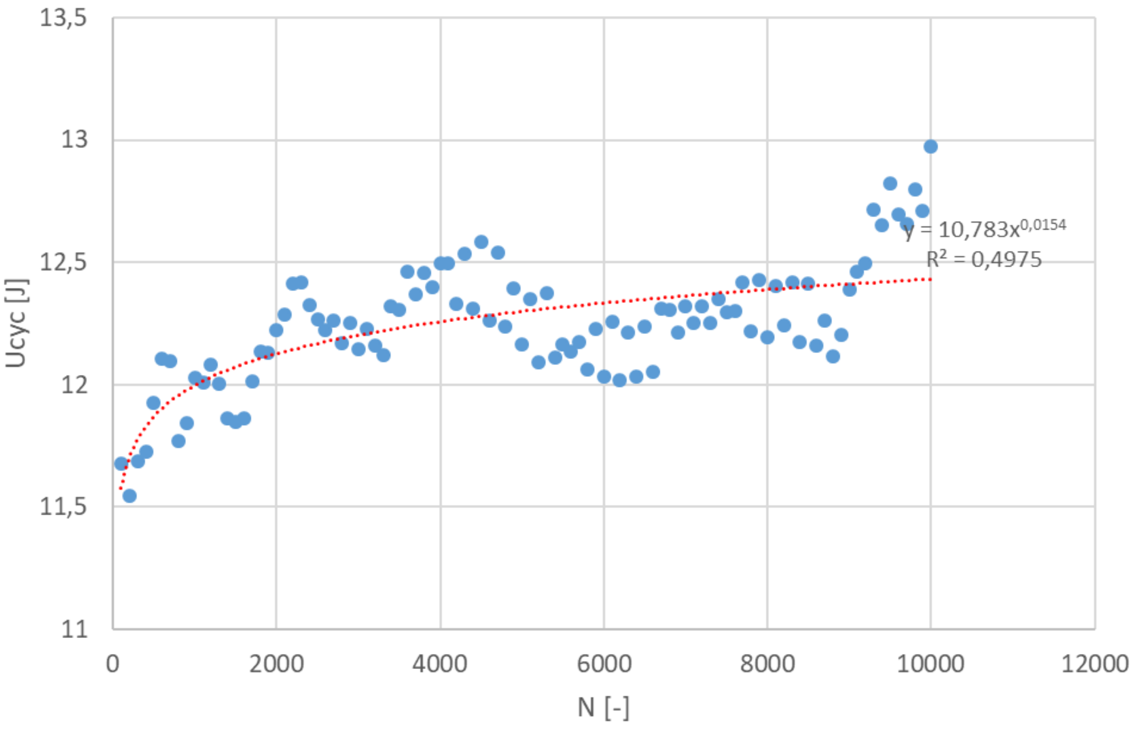

Figure 4.13: Cyclic work versus amount of cycles for angle-ply coupons tested with a maximum load of 18 kN

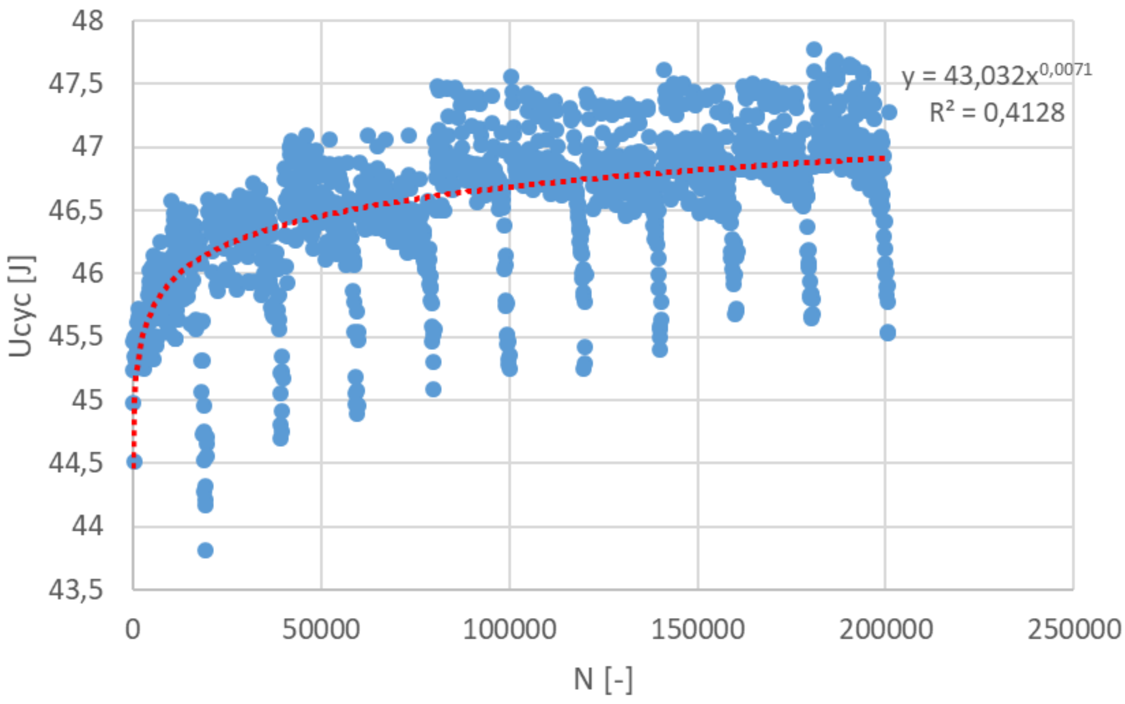

Figure 4.14: Cyclic work versus amount of cycles for quasi-isotropic coupons tested with a maximum load of 52 kN

It can be seen that there is scatter for each lay-up, this may be due inaccuracies in the measurement of the loads and displacements during the cycles. The unidirectional, cross-ply and quasi-isotropic lay-ups start with a steep increase in the beginning after which the slope continuously decreases and the curve eventually levels off, except for quasi-isotropic which continues to increase. The curve for the coupons with a 45°/-45° lay-up continuously increased until end-of-life, which means the continued increase in cyclic work in the quasi-isotropic curves were caused by the 45° and -45° plies.
As the minimum and maximum loads were kept constant, an increase in cyclic work means an increase in displacement and a change in slope for the load displacement curve, which means a decrease in laminate stiffness over time.
The decrease in laminate stiffness is caused by damage initiation and growth in the coupons. The cyclic work appear to follow a similar trend as the crack growth for unidirectional and cross-ply lay-up.

To check for a relation between displacement and crack length the maximum displacement measured by the test bench was plotted versus the crack length as shown in figures 4.15 to 4.18. It can be seen that the maximum displacement rapidly increases in the beginning, but the effect of the crack growth on the displacement diminishes over time for the fibre splits in the unidirectional and quasi-isotropic coupons. The matrix cracks in 45° and -45° directions in the angle-ply coupons followed a similar trend. As the 45° and -45° plies failed before the 0° plies in quasi-isotropic coupons, only the initial increase in displacement was affected by the matrix cracks.
For cross-ply coupons as shown in figure 4.16, the displacement does not appear to be related to the crack length, but this may be caused by inaccuracy in the displacement measurements from the test bench.

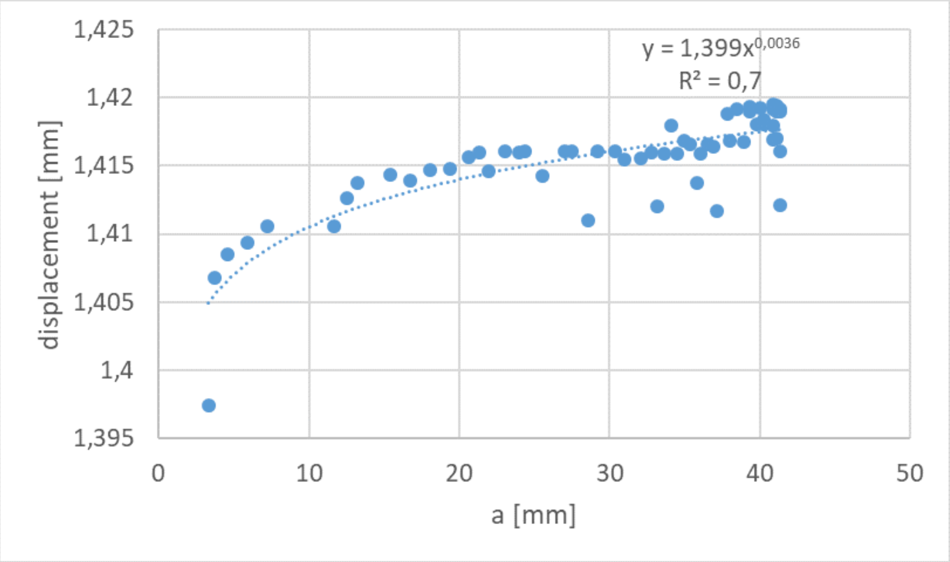

Figure 4.15: Measured maximum displacement versus the crack length a for unidirectional coupon tested with a maximum load of 53 kN

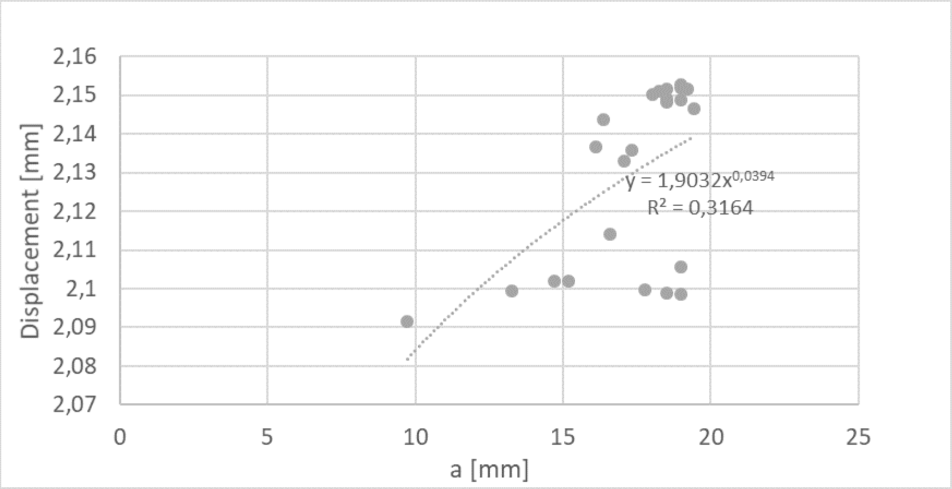

Figure 4.16: Measured maximum displacement versus the crack length a for cross-ply coupon tested with a maximum load of 60 kN

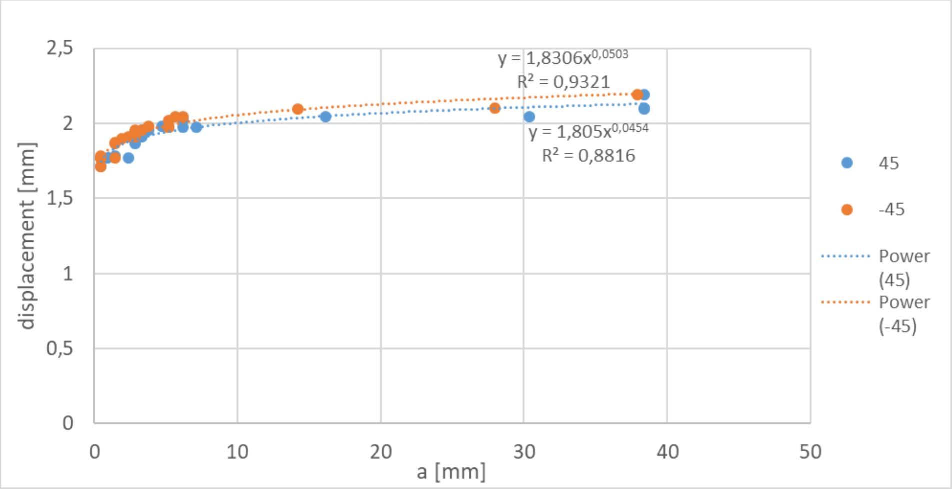

Figure 4.17: Measured maximum displacement versus the crack length a for angle-ply coupon tested with a maximum load of 18 kN

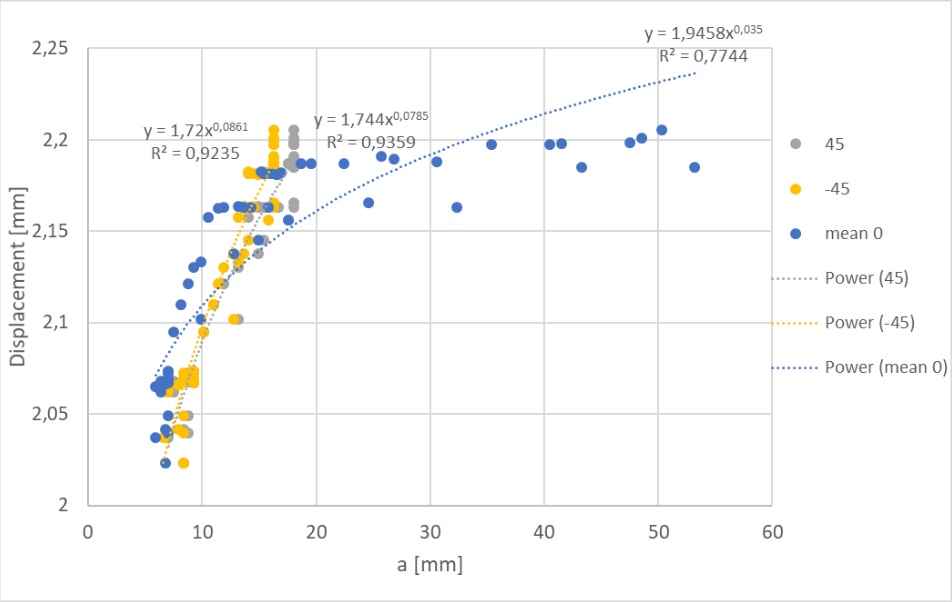

Figure 4.18: Measured maximum displacement versus the crack length a for quasi-isotropic coupon tested with a maximum load of 52 kN

For calculating the displacement it was assumed that the maximum displacement during the cycle occurred at the same point as the maximum load that was measured, due to the linear elasticity of composites. The calculated displacement can be found in figures 4.19 to 4.21

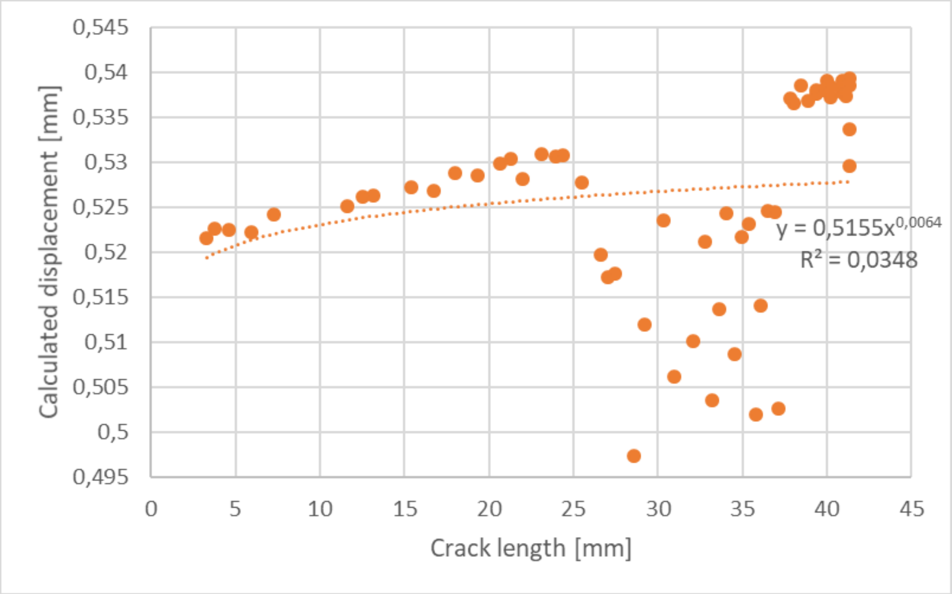

Figure 4.19: Calculated maximum displacement versus crack length a for the coupon with unidirectional lay-up tested at maximum load 53 kN

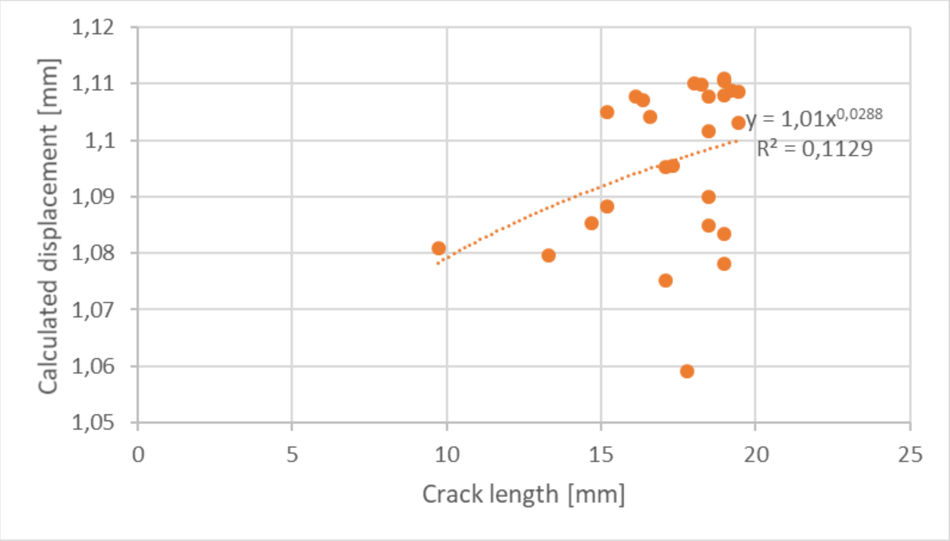

Figure 4.20: Calculated maximum displacement versus crack length a for the coupon with cross-ply lay-up tested at maximum load 62 kN

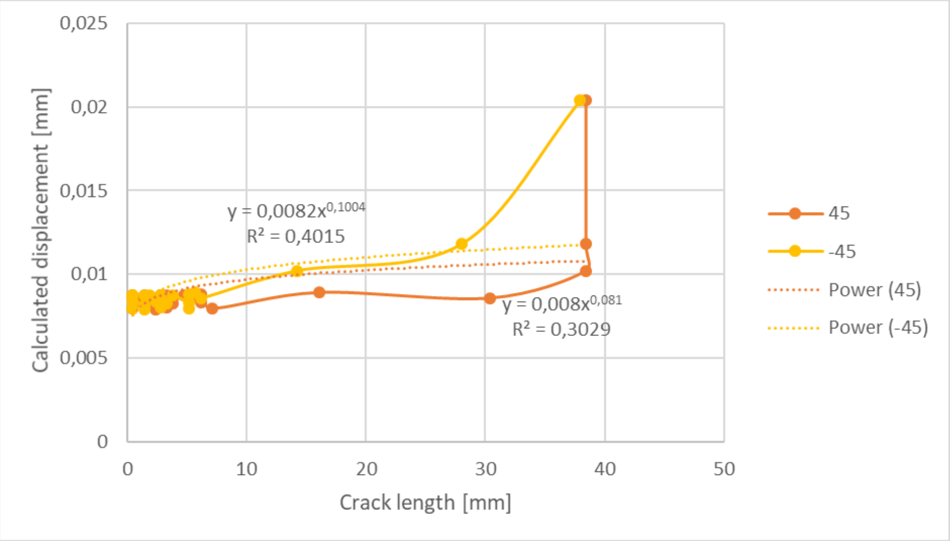

Figure 4.21: Calculated maximum displacement versus crack length a for the coupon with angle-ply lay-up tested at maximum load 18 kN

Comparing the measured displacement to the calculated displacement it can be seen that both follow a similar trend, however there is an offset between them. This suggests that there is indeed a relation between displacement and crack length. The offset is most likely due to the test bench measuring the displacement of the test bench and not just the displacement of the coupon. Therefore, the displacement measurements included the stiffness from the test bench, while the calculated displacement only takes the approximated coupon stiffness into account, which caused the offset in displacement. The amount of scatter found for both the measured and calculated displacement could be due to the scatter in maximum load measured during each cycle, as the measured load was not exactly the same for each measured cycle. This also explains the scatter found in the cyclic work.

The difference between measured displacement and calculated displacement for angle-ply is caused by a change in stiffness during the test due to the matrix cracks growing, while during the calculations of the displacements the stiffness of the angle-ply coupons was kept constant.
Since the overall trends of the measured and calculated displacements are the same, the calculated cyclic work trends will be the same, but the actual values will be lower.
The SERR depends on the trend between displacement and crack length and would therefore not be affected by the difference between measured and calculated displacement.
The dissipated energy is based on the hysteresis loop of a load cycle. As only the maximum displacement was investigated and not an entire load cycle it can not be said how the difference would affect the dissipated energy calculations.

Then using the relations found between the displacement and the crack length, the strain energy release rate was calculated using equation 3.5 and plotted versus the crack growth rate da/dN as shown in figures 4.22 to 4.25.
There is an increasing power relation between the strain energy release rate and the crack growth rate for fibre splitting in the unidirectional and cross-ply coupons. For the matrix cracks in angle-ply coupons the crack growth decreases with increasing strain energy release rate. Comparing this to the crack growth shown in figure 4.3, more strain energy is released to initiate the crack growth after which less strain energy has to be released to continue the growth.
For the quasi-isotropic coupons an increasing power relation was found for the matrix cracks in 45° and -45° directions, however for the crack growth in the 0° plies the slope is similar to the 45° and -45° cracks when the growth of the matrix cracks was dominant. When the crack growth in the 0° plies was dominant the slope changed.

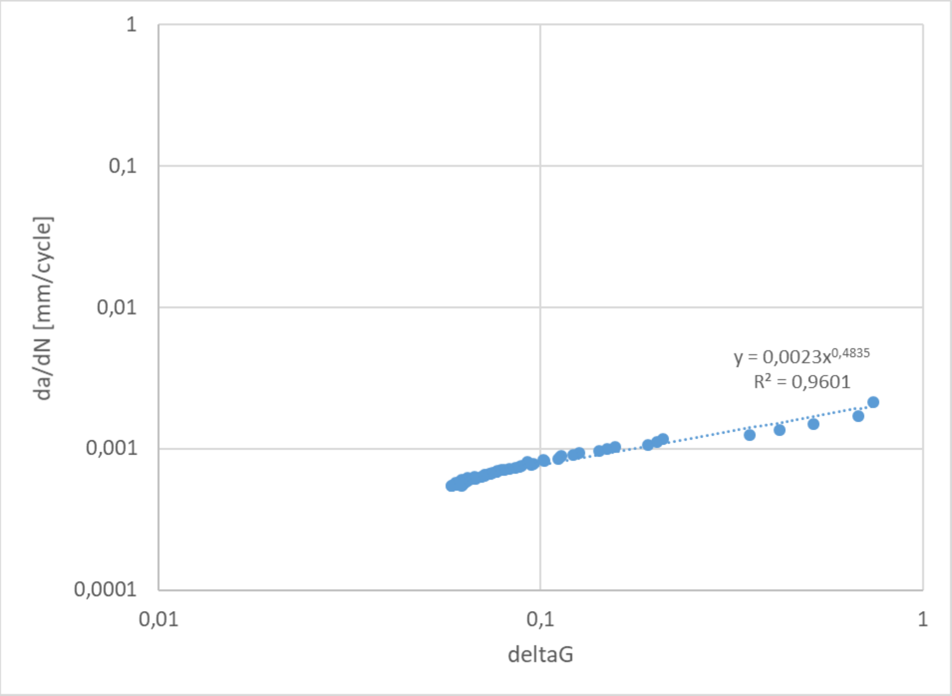

Figure 4.22: Crack growth da/dN versus the similitude parameter $\Delta G = \left(\sqrt{G_{max}} - \sqrt{G_{min}}\right)^2$ for unidirectional coupon with a maximum load of 53 kN

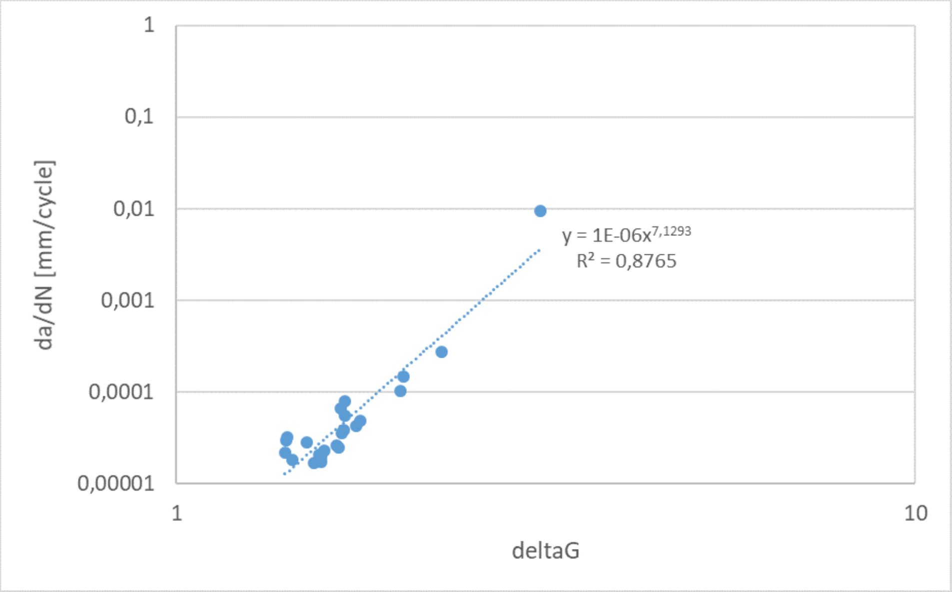

Figure 4.23: Crack growth da/dN versus the similitude parameter $\Delta G = \left(\sqrt{G_{max}} - \sqrt{G_{min}}\right)^2$ for cross-ply coupon with a maximum load of 60 kN

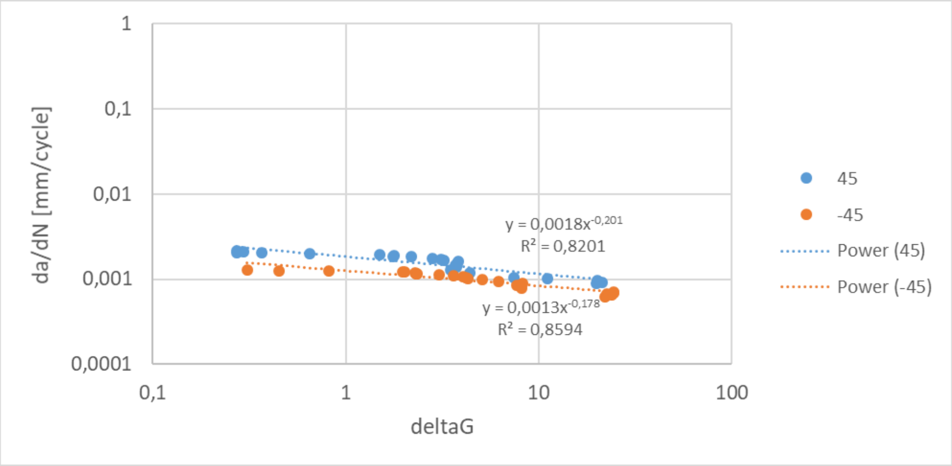

Figure 4.24: Crack growth da/dN versus the similitude parameter $\Delta G = \left(\sqrt{G_{max}} - \sqrt{G_{min}}\right)^2$ for angle-ply coupon with a maximum load of 18 kN

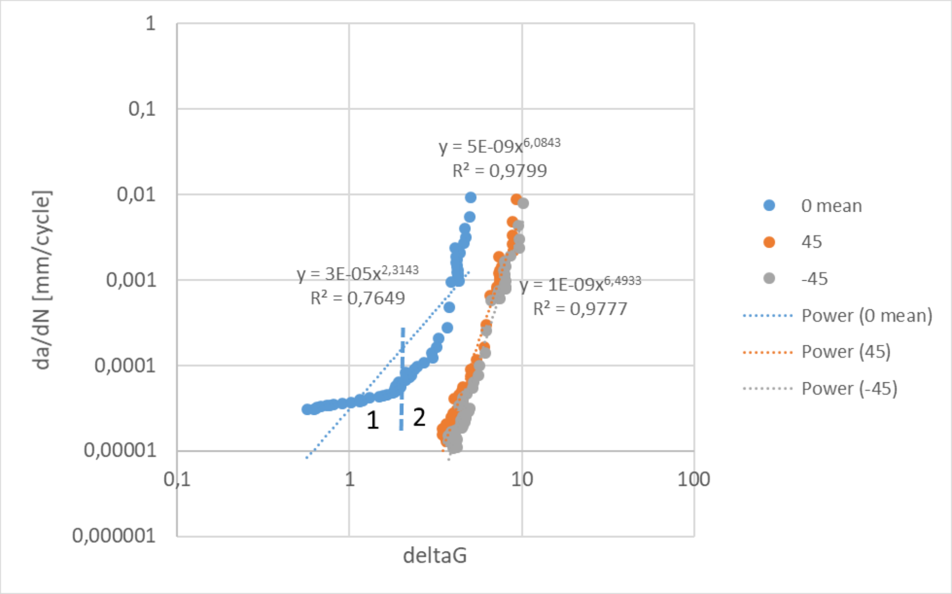

Figure 4.25: Crack growth da/dN versus the similitude parameter $\Delta G = \left(\sqrt{G_{max}} - \sqrt{G_{min}}\right)^2$ for quasi-isotropic coupon with a maximum load of 52 kN. A line was drawn through the curve for crack growth in the 0° plies. Part 1 of the curve was when fibre splitting was dominant, while in part 2 matrix cracks were dominant.

To see if the cyclic work can be correlated to the strain energy release rate the cyclic work per cycle was plotted versus the crack growth rate, as shown in figures 4.26 to 4.29.
The unidirectional, cross-ply and angle-ply coupons have similar trends as the strain energy release rate. The quasi-isotropic coupons have similar trends for the matrix cracks in 45° and -45° directions, but not for the fibre splits in 0° direction.

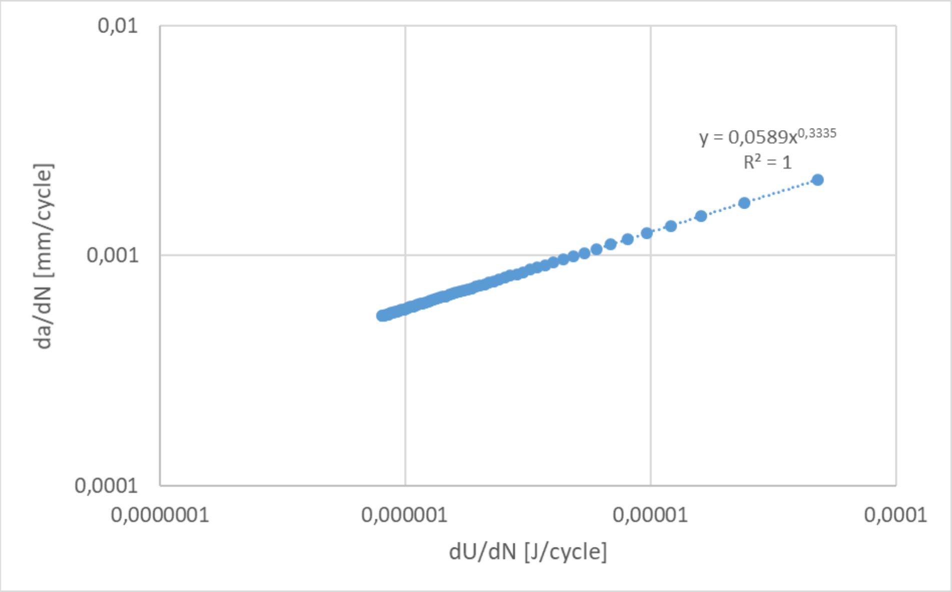

Figure 4.26: Crack growth da/dN versus the cyclic work per cycle dU/dN for unidirectional coupon with maximum load of 53 kN

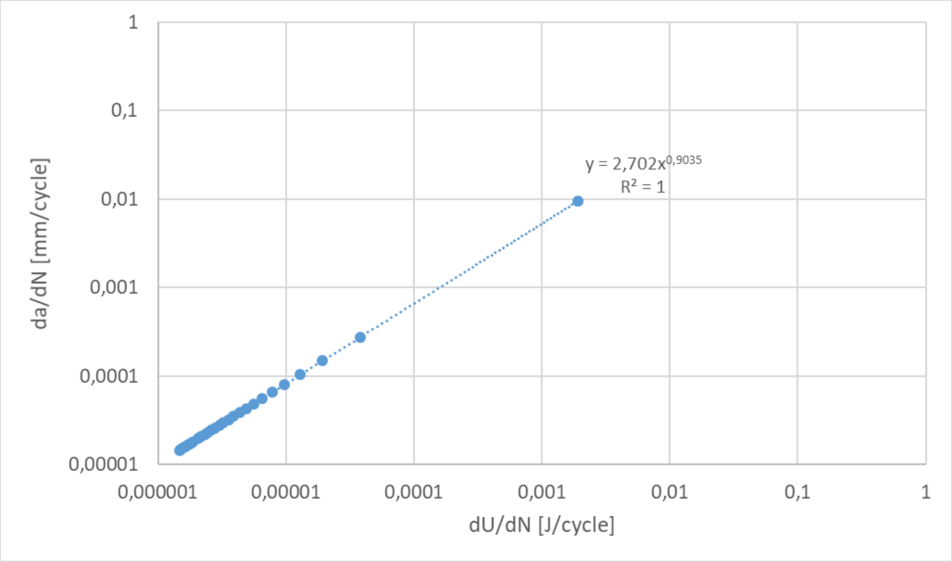

Figure 4.27: Crack growth da/dN versus the cyclic work per cycle dU/dN for cross-ply coupon with maximum load of 60 kN

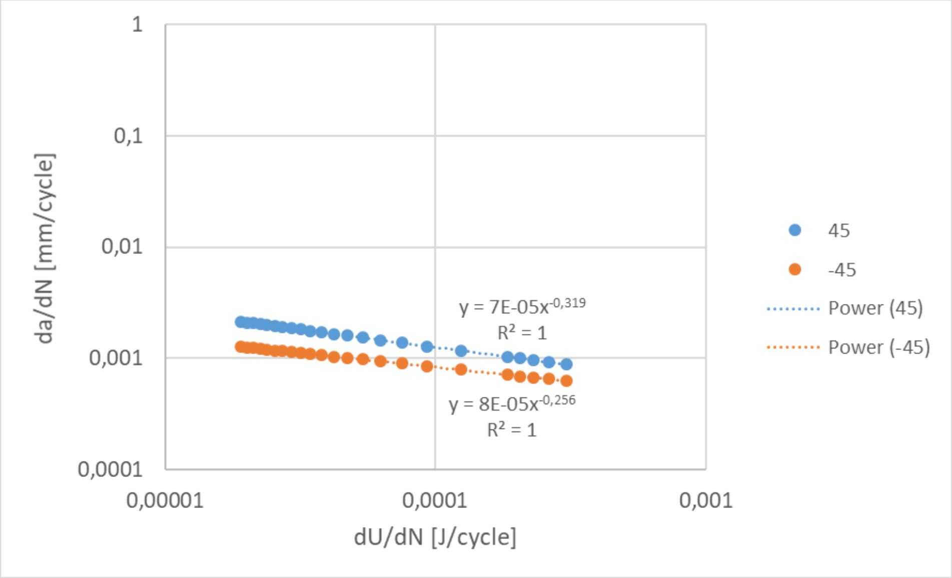

Figure 4.28: Crack growth da/dN versus the cyclic work per cycle dU/dN for the angle-ply coupon with maximum load of 18 kN

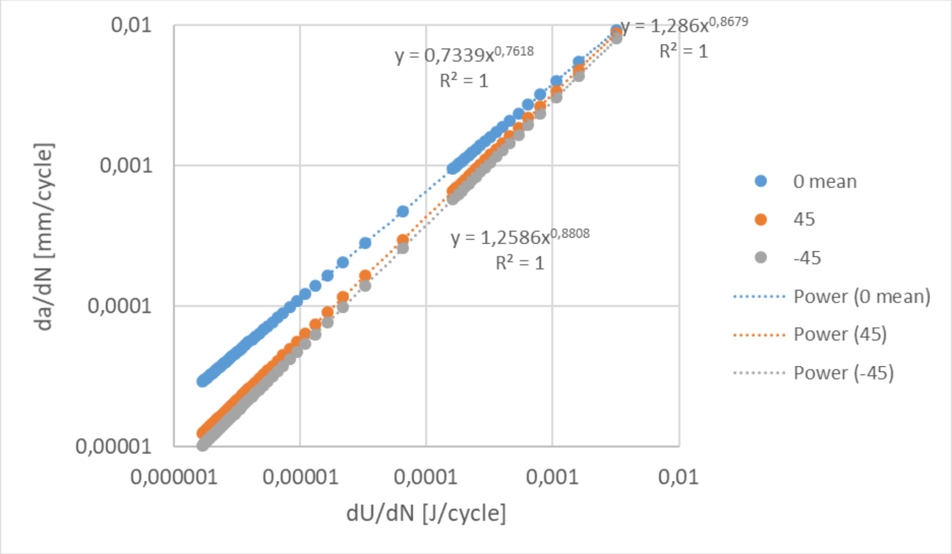

Figure 4.29: Crack growth da/dN versus the cyclic work per cycle dU/dN for the quasi-isotropic coupon with maximum load of 52 kN

The dissipated energy data had outliers at the same cycles as the cyclic work, the values were either NaN or much higher than the values of the nearby data points. The cause is the same as for the cyclic work, so these data points were disregarded.

The dissipated energy versus number of cycles for each lay-up is shown in figures 4.30a and 4.30d. There is no distinguishable difference in behaviour for the dissipated energy between lay-ups and there is a large amount of scatter between data points, so no trend could be determined. This is mostly caused by the inaccuracy in the load-displacement data and more accurate tools should be used to determine the dissipated energy.

Only the angle-ply and quasi-isotropic coupons show a slight decrease over time in dissipated energy, thus the decrease in stiffness in the unidirectional and cross-ply was not significant enough to cause a decrease in dissipated energy.
Comparing the dissipated energy versus the number of cycles with the crack length versus number of cycles it was found that for the angle-ply coupons the initial peak happened around the same time as the beginning of crack growth suggesting that when matrix cracks initiate more energy is dissipated. For the quasi-isotropic coupon the peak of dissipated energy is around the time the cracks in the 45° and -45° plies started to reach the end of the specimen, which is also when damage interactions occur initiating delamination in the inner delamination regions, as described by Green et al [21].

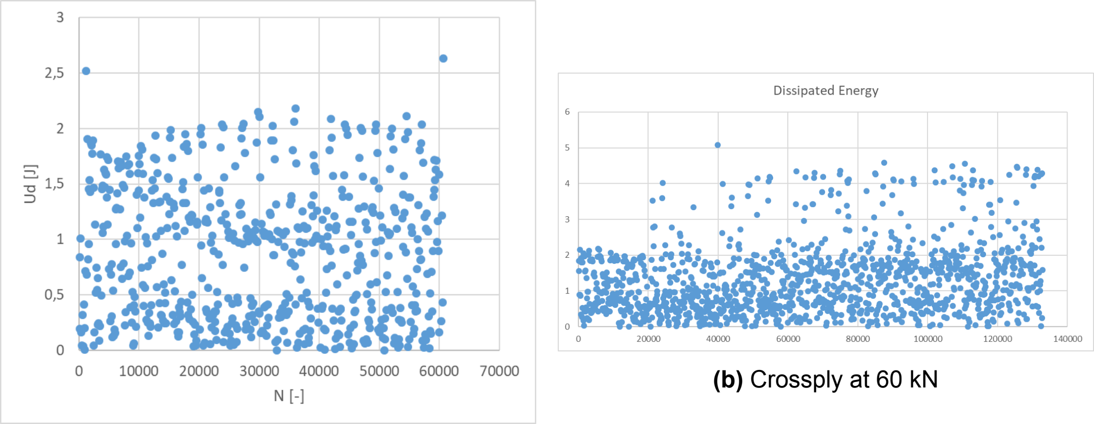

(b) Crossply at 60 kN

(a) UD at 53 kN

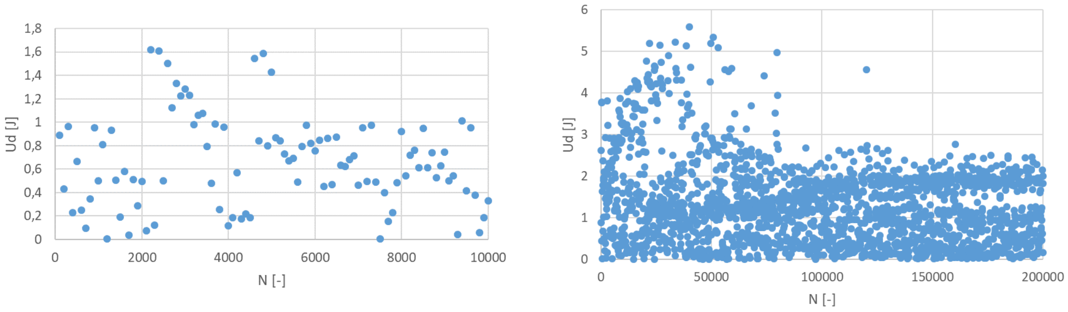

(c) Angleply at 18 kN

(d) QI at 52 kN

Figure 4.30: Dissipated energy versus amount of load cycles for lay-ups unidirectional (UD), angle-ply, cross-ply and quasi-isotropic (QI)

However, when plotting the total amount of energy dissipated versus the number of cycles to failure, there appears to be a linear relation between the lifetime of a composite specimen and the amount of energy dissipated during a coupon's life.

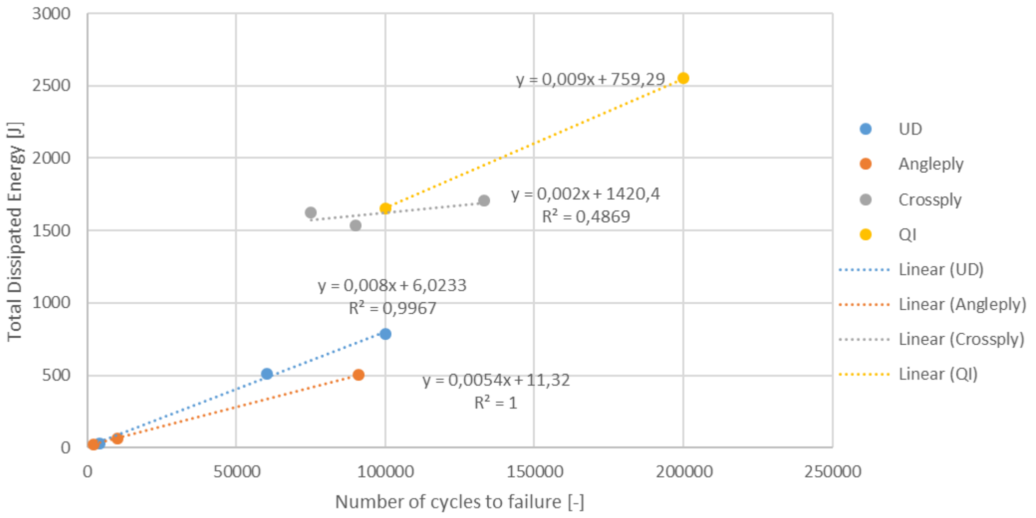

Figure 4.31: Total dissipated energy versus number of cycles to failure for the lay-ups unidirectional (UD), angle-ply, cross-ply and quasi-isotropic (QI). Trend-lines were drawn between the data points indicating a linear relation between total dissipated energy and number of cycles until failure.

4.3. Acoustic Emission Data

After applying the filter to the data as described in section 3.3, the cumulative energy and amount of hits registered were calculated at intervals of 20s, which equals approximately 100 cycles per interval. To plot the cumulative energy and hits, the time in seconds for each data point had to be converted to number of cycles. This was done using the following piece of code:

```
Step 1: Set ti to 0
Step 2: Calculate the number of cycles with
N = (t[i]-t[0]-ti*0.5)*5 where i is the index of the current cycle
and 0 the index of the first cycle.
Step 3: If N is larger than (ti+1)*100,
then ti is increased by 1 and N is recalculated.
Repeat step 2 and 3 until the last cycle.
```

In figures 4.32 to 4.35 the cumulative number of acoustic emission hits registered versus amount of cycles is shown. For unidirectional coupons there are three different areas visible in figure 4.32. First a steep increase when the cracks initiate at the start followed by a lower slope as the cracks continue to grow. As the crack grow closer to the acoustic emission sensors, the slope starts to increase.

The crossply coupons have a similar trend as the unidirectional coupons had the crack growth is in the same direction. It is assumed that most of the matrix cracking in the 90° layers occurred during the first couple of cycles and does not influence the overall trend of the accumulated number of hits.

For angleply coupons the number of hits registered slowly increases at the start and near the end-of-life starts to rapidly increase, as shown in figure 4.34, similarly to the crack growth shown in figure 4.3. The change in slope occurs around the number of cycles the when the coupon started to elongate around the hole.

For the quasi-isotropic coupon the slope of the curve increases as the cracks grows. Possibly initially due to growth of the cracks in the 45° and -45° plies followed by the growth of the fibre splits in 0° direction.

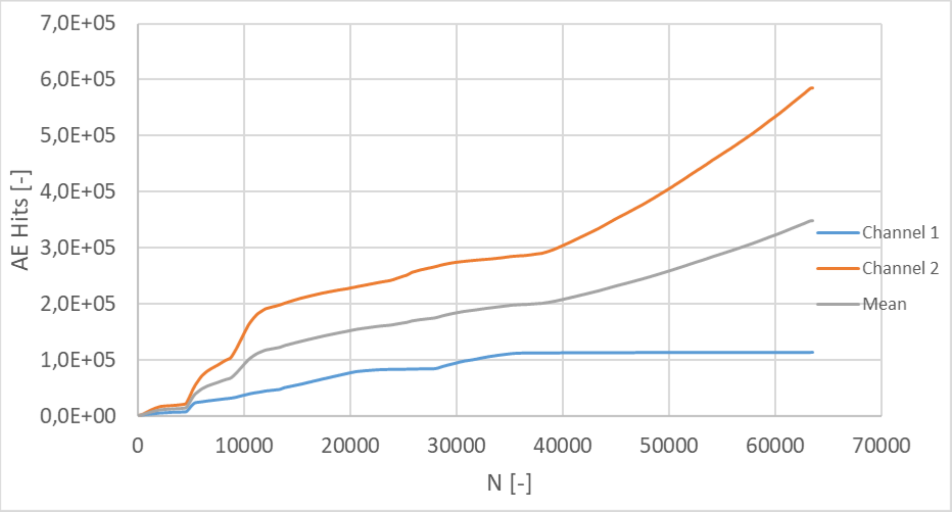

Figure 4.32: Cumulative number of acoustic emission hits versus amount of load cycles for unidirectional coupon with a maximum load of 53 kN

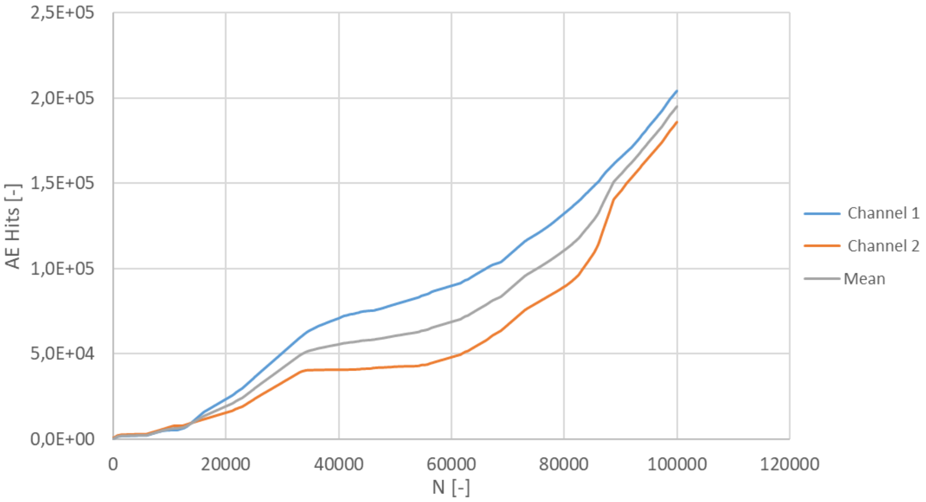

Figure 4.33: Cumulative number of acoustic emission hits versus amount of load cycles for cross-ply coupon with a maximum load of 60 kN

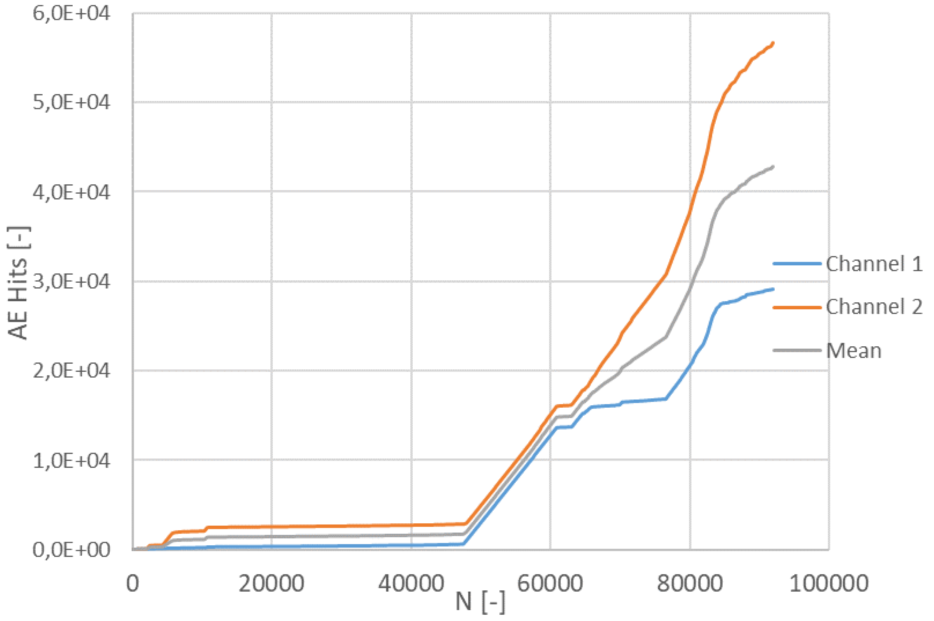

Figure 4.34: Cumulative number of acoustic emission hits versus amount of load cycles for angle-ply coupon with a maximum load of 18 kN

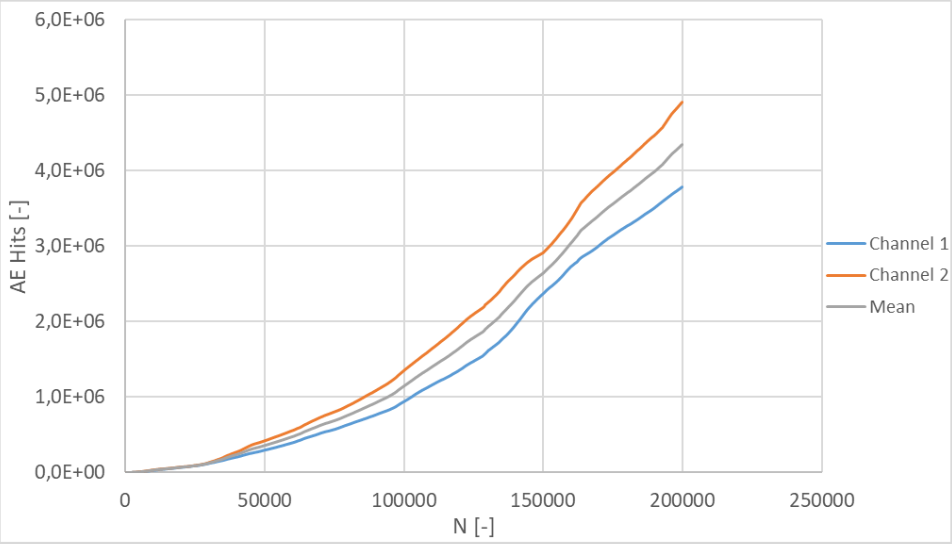

Figure 4.35: Cumulative number of acoustic emission hits versus amount of load cycles for quasi-isotropic coupon with a maximum load of 52 kN

The differences between channel 1 and channel 2 is due to hits being filtered out based on their amplitude, which decreases as the distance between the sensor and the damaging event increases [32]. Therefore, for comparing the hits and energy with the crack length, the mean between the two channels was used.

In figures 4.36 to 4.39 the cumulative acoustic energy versus amount of cycles are shown. It can be seen in figures 4.36 and 4.38 that for the unidirectional and angleply coupons the acoustic hits and acoustic energy follow similar trends as the acoustic hits and crack length.

The coupons with crossply lay-up slowly increases until the fibre splits are close to the edge of the DIC area, after which there is a change in slope. Acoustic energy is determined using the amplitude and duration of the acoustic hits, so the acoustic emission features have to be investigated to determine the cause.

The acoustic energy measured for quasi-isotropic coupons slowly increases at the beginning and changes slope when the cracks in the 45° and -45° aproach the edges of the coupon and the rate at which the fibre splits in the 0° plies starts to increase. This suggest that fibre splits emit more acoustic energy than matrix cracks.

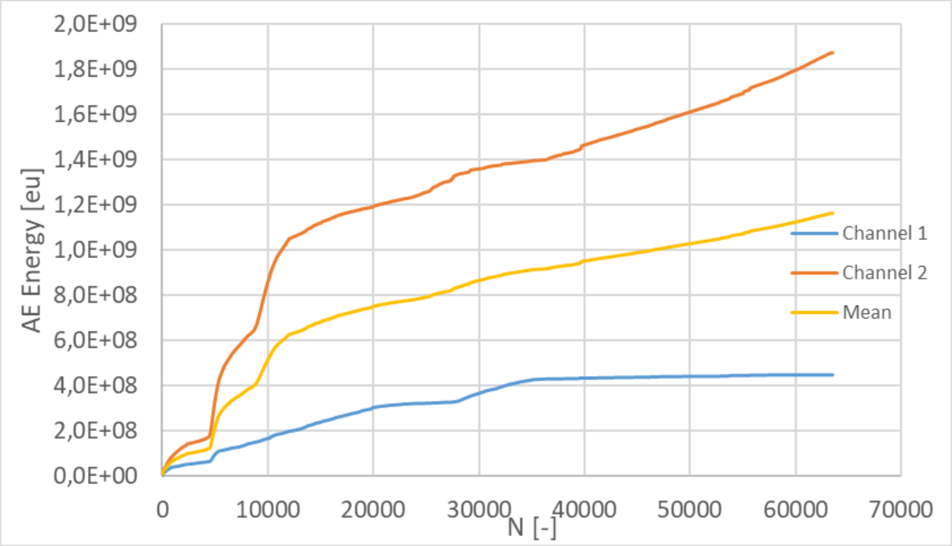

Figure 4.36: Cumulative acoustic emission energy versus amount of load cycles for unidirectional coupon with maximum load of 53 kN

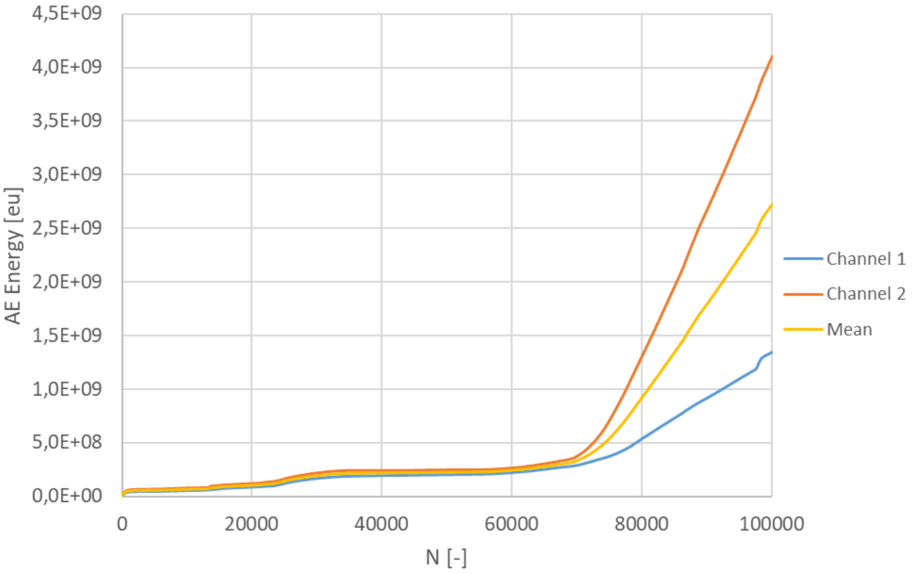

Figure 4.37: Cumulative acoustic emission energy versus amount of load cycles for cross-ply coupon with maximum load of 62 kN

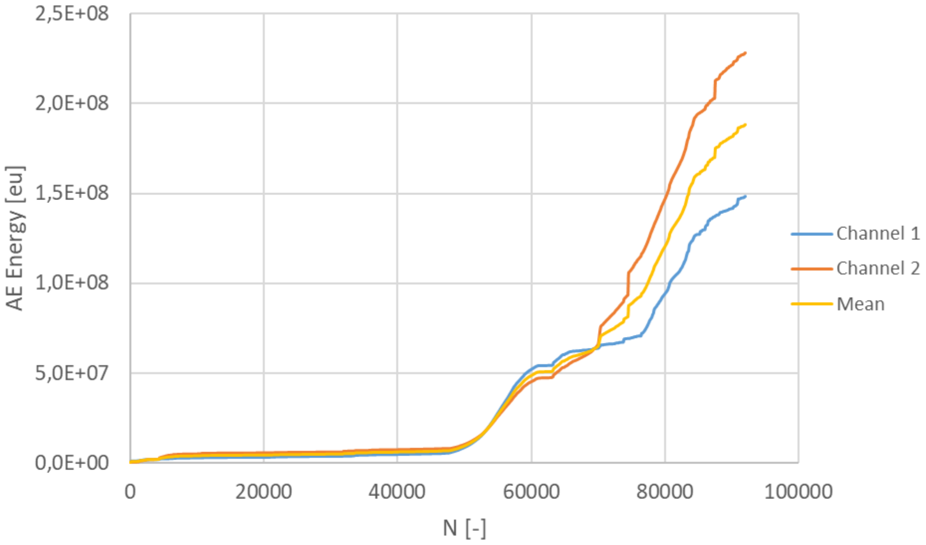

Figure 4.38: Cumulative acoustic emission energy versus amount of load cycles for angle-ply coupon with maximum load of 16 kN

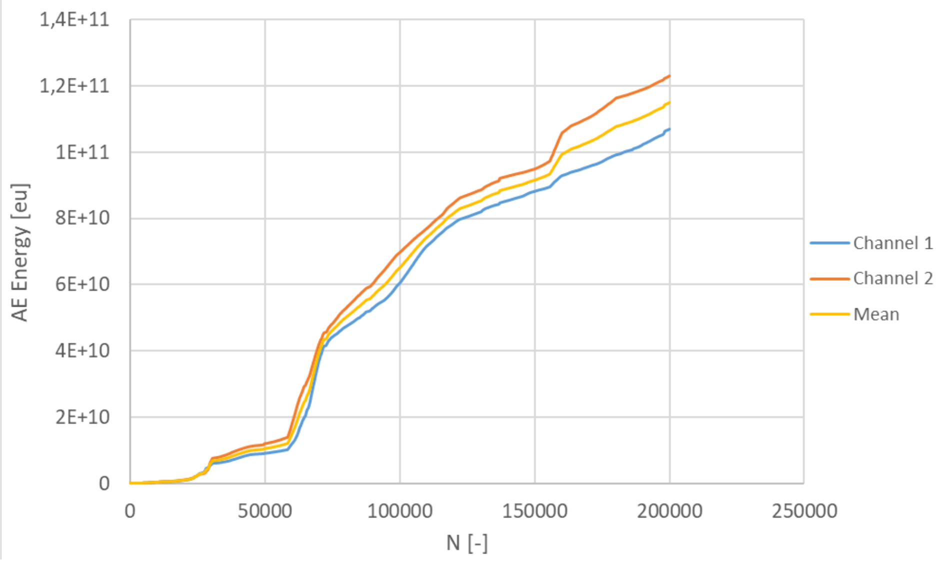

Figure 4.39: Cumulative acoustic emission energy versus amount of load cycles for quasi-isotropic coupon with maximum load of 52 kN

In order to determine if unique features related to the damage growth could be identified, the acoustic emission features rise time, duration and amplitude were investigated by plotting the rise time and duration versus the amplitude for each channel. Then the data points were divided based on the load ranges they were measured.

The load ranges were 0-10% of maximum load, 10-25% of maximum load, 25-50% of maximum load, 50-75% of maximum load and 75-100% of maximum load. Since the test range was from 10-100% of maximum load any data points below 10% will most likely be due to starting and stopping the tests. It was found that the number of hits below 10% maximum load was below 1% for most coupons and the percentage decreased as number of cycles measured increased.

As shown in figures 4.40 and 4.41, it was found that between 75% and 100% maximum load, damage growth in UD coupons can be characterised by low rise time below 100 μs, high amplitude and duration above 100 μs, which corresponds with what was found in [5]. The hits found during lower load levels can be attributed to friction based mechanisms, which are most prominent during fatigue tests with stress ratio R = 0.1 [49].

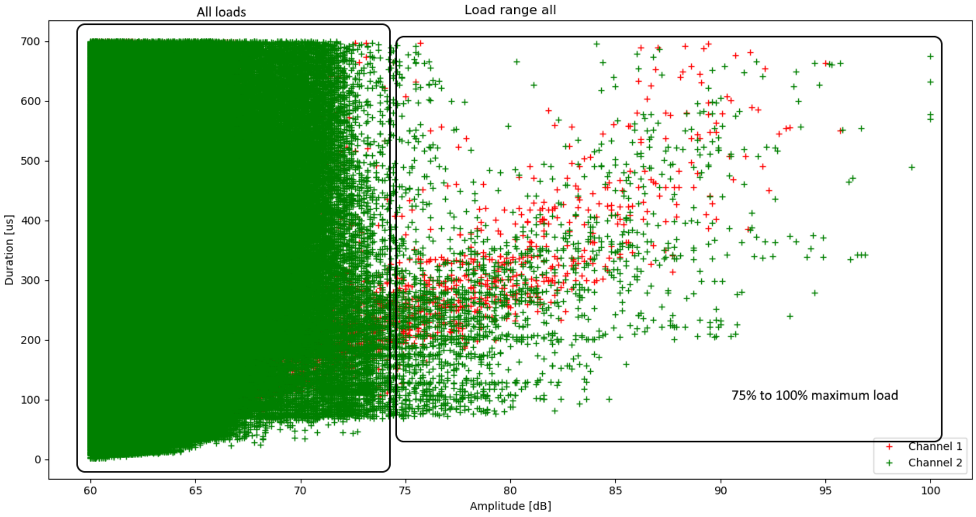

Figure 4.40: Duration versus amplitude for the coupon with UD lay-up and a maximum load of 53 kN

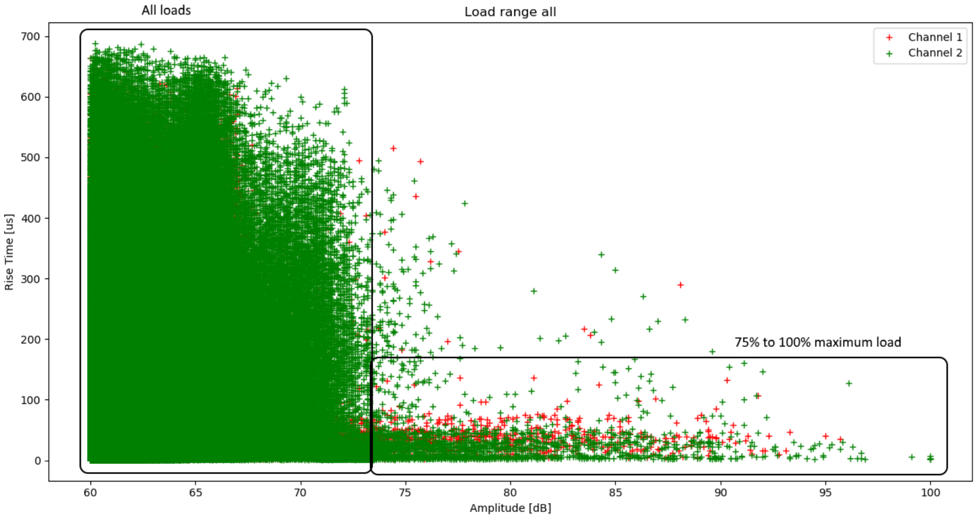

Figure 4.41: Rise time versus amplitude for the coupon with UD lay-up and a maximum load of 53 kN

In figures 4.42 and 4.43 it can be seen that damage growth could be found for loads between 50% and 100% maximum load with a medium to high duration (200 to 900 μs), high amplitude (80 to 100 dB) and low to high rise time (0 to 500 μs).

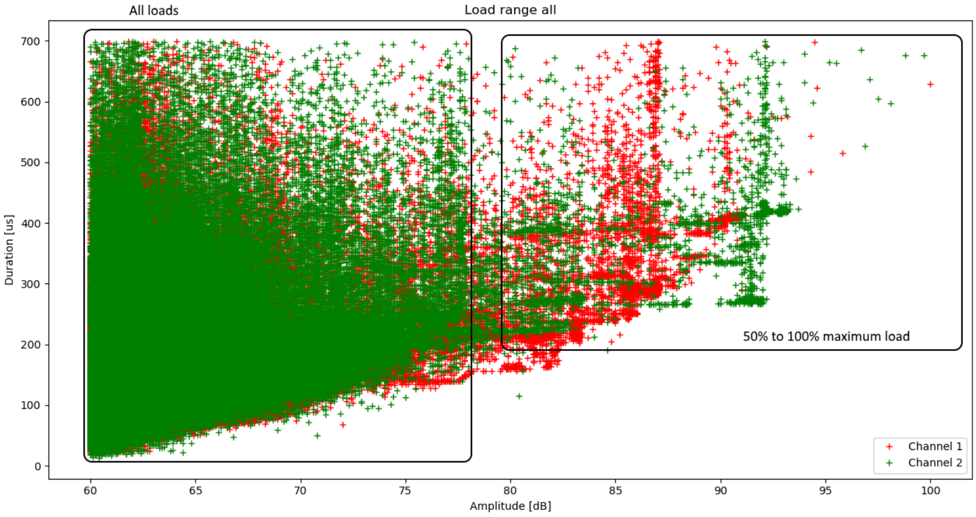

Figure 4.42: Duration versus amplitude for the coupon with angleply lay-up and a maximum load of 18 kN

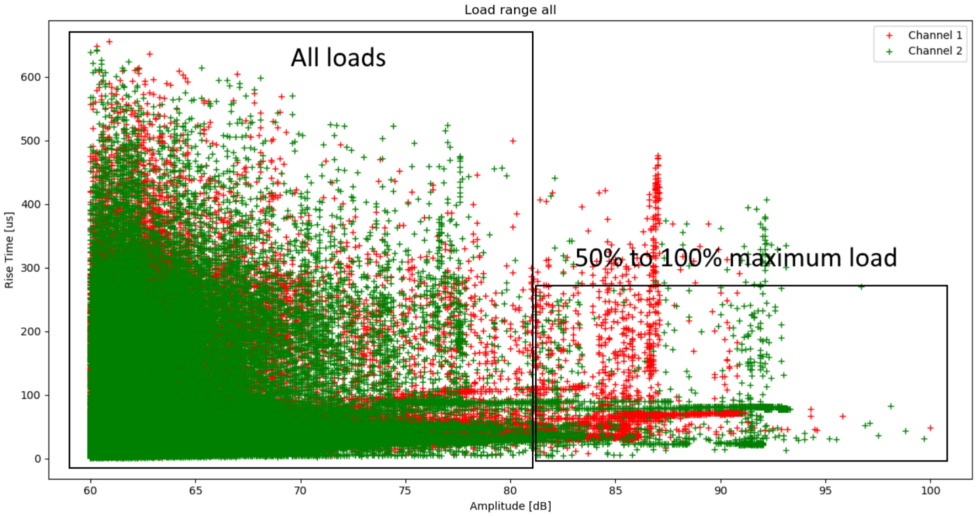

Figure 4.43: Rise time versus amplitude for the coupon with angleply lay-up and a maximum load of 18 kN

For crossply coupons the damage acoustic features for damage growth could be found for loads between 75% and 100% maximum load, as shown in figures 4.44 and 4.45. The damage growth occurred for acoustic hits with medium to high duration (300 to 900 μs), high amplitude (80 to 100 dB) and low to medium rise time (0 to 300 μs).
These described features could not be distinguished individually in the quasi-isotropic coupons. To better relate the crack growth data with the acoustic emission features, the acoustic emission data could possibly also be divided based on the range of cycles in which the acoustic hits occurred. This way the

damage mechanisms could possibly be distinguished in the quasi-isotropic coupons by comparing the time of occurrence for the acoustic hits with the crack growth data.
Another possibility is to use pattern recognition techniques to distinguish patterns from the acoustic feature plots, to better chart the characteristics for damage mechanisms in the coupons with unidirectional, crossply and angle-ply lay-up. This could then be used to distinguish the damage mechanisms in the acoustic emission data for quasi-isotropic coupons.
Another improvement would be to use frequency based analysis instead of amplitude based analysis [22], as the amplitude depends on the distance between the acoustic sensors and the acoustic event and the damage grew in the direction of the sensors.

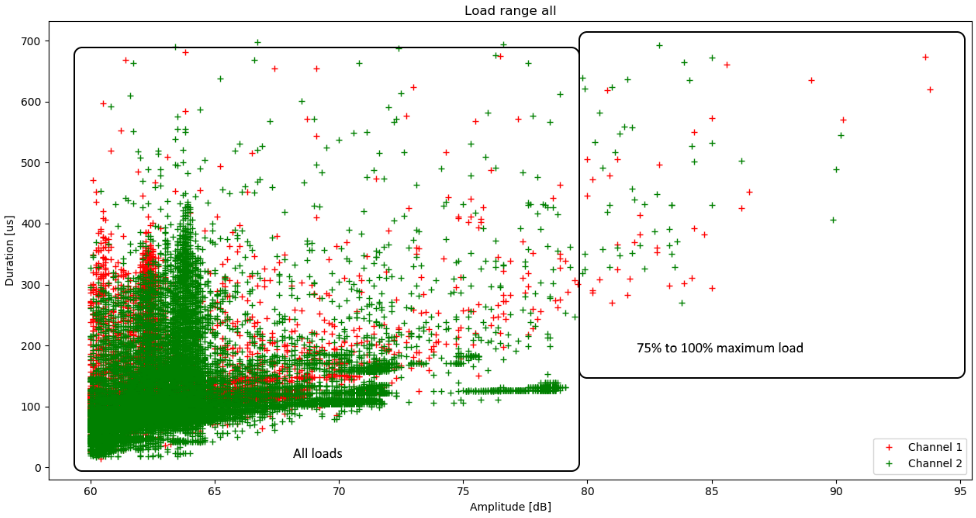

Figure 4.44: Duration versus amplitude for the coupon with crossply lay-up and a maximum load of 60 kN

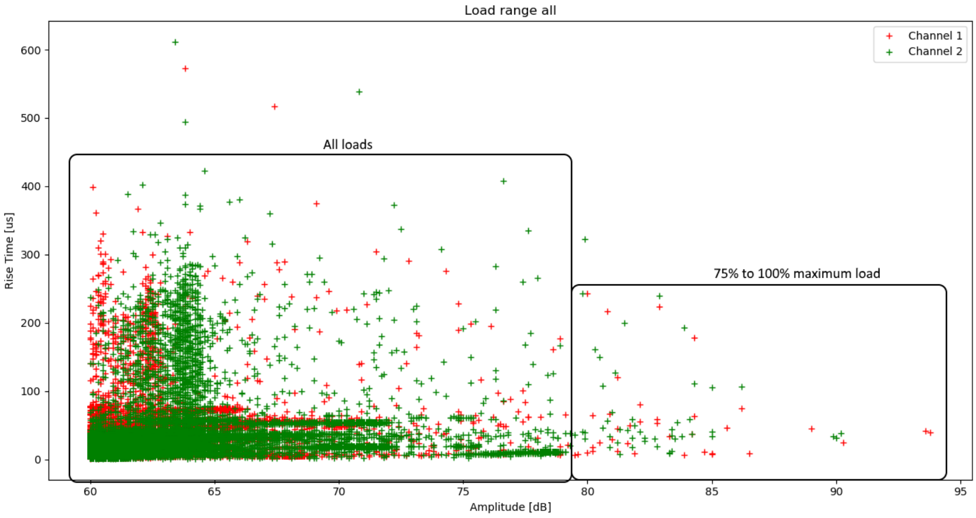

Figure 4.45: Rise time versus amplitude for the coupon with crossply lay-up and a maximum load of 60 kN

It was also investigated whether a load threshold can be found for which the damage mechanisms are visible in all coupons with the same lay-up. This was done by increasing the load at which the features were plotted and searching for patterns that indicate damage growth. For unidirectional coupons this threshold was for loads around 70% of the maximum load. For crossply coupons the threshold was found for loads around 50% of the maximum load and for angleply coupons the threshold was for loads around 70% of the maximum load.

5

Conclusions and Recommendations

5.1. Conclusions

Various different models have been developed over the years to predict the fatigue life of composites. However, these models are phenomenological and are incapable of accurately explaining the behaviour of composites during fatigue. A connection was found between dissipated energy and damage mechanism, which could be used to create a model for constructing fatigue life curves that are based on the damage mechanisms in composites.

It was found that in a quasi-isotropic laminate there are different fracture modes in the 0° plies, the 90° plies and the ±45° plies. These fracture modes grow independently of each other at the start. Therefore, they can investigated individually by testing coupons with a 0°, 0/90° and 45/-45° lay-up.

To isolate the damage mechanisms three different lay-ups were tested: unidirectional $[0_{24}]$, crossply $[(0/90)_6]_s$ and angleply $[(45/-45)_6]_s$. To investigate the effect of the interactions between the different damage modes, coupons with quasi-isotropic lay-up $[(0/90/45/-45)_3]_s$ were tested. The coupons were tested for tension-tension fatigue using a MTS 100 kN fatigue machine with stress ratio R = 0.1 and frequency f = 5 Hz. During the tests the displacement and force were measured using the sensors in the test bench, acoustic emission sensors were clamped to the specimen to perform acoustic emission measurements and two cameras would take pictures every 100th cycle for digital image correlation (DIC).

Fibre splitting was found in the coupons with unidirectional and crossply lay-ups. The growth of the matrix cracks in the 90° plies could not be measured as these cracks reached the edge of the coupon within 100 cycles. The matrix cracks found in the coupons with angleply lay-up started from the centre of the open hole and grew in 45° and -45° directions to the edge of the coupon, after which the the coupon started to delaminate near the hole. Both the fibre splitting and the matrix cracking were found in the quasi-isotropic coupons. Out-of-plane delamination appeared between the fibre split lines at the edge of the hole.

Using the displacement and load measurements from the test bench, the cyclic work was calculated by determining the area underneath the first half of a load cycle. The dissipated energy was determined by determining the area underneath the first half and subtracting the area of the second half of the load cycle in order to calculate the area in the hysteresis loop. This was done for every 100th cycle.
The cyclic work for coupons with unidirectional, crossply or quasi-isotropic lay-up start with a steep increase after which the slope decreases. For unidirectional and crossply the increase appears to be asymptotic, while the quasi-isotropic coupons still continue to increase. The cyclic work for coupons with angleply lay-up increases continuously with increasing number of cycles. As the maximum and minimum load were kept constant, the increase in cyclic work was caused by an increase in difference between minimum and maximum displacement, which indicates an increase in compliance over time for angleply and quasi-isotropic. Plotting the maximum displacement versus the crack length showed that there is indeed a relation between crack length and displacement, however the effect of crack length on the displacement decreases as the crack grows.

The relation between displacement and crack length was used to determine the strain energy release rate for the different coupons. Comparing the strain energy release rate with to the cyclic work and crack growth, the strain energy release rate showed similar trends as the cycle work related to crack growth. The distribution of dissipated energy over time appears to not be related to the damage mechanisms found with digital image correlation, however the total amount of dissipated energy is related to the number of cycles until failure.

The data from the acoustic emission measurements was first filtered based on amplitude, rise time and duration of the acoustic hits. Afterwards, the cumulative number of hits and amount of acoustic energy measured were calculated and plotted versus the number of cycles for each channel. There is a difference in amount of hits registered between channels, due to the hits being filtered based on amplitude, which depends on the distance between a sensor and the acoustic event.

In the unidirectional and crossply coupons three different areas could be identified: a steep increase as the crack started to grow followed by decreased slope as the cracks continued to grow, after which a change in slope occurs when the cracks approach the sensors due to distance between the cracks and acoustic sensors decreasing.
To identify damage mechanisms using acoustic emission features, the acoustic hits rise time and duration were plotted versus the amplitude for each channel. The hits were then separated based on their loads. Hits with low load level are mostly caused by friction based mechanisms that are prominent for low stress ratios.
In coupons with unidirectional lay-up, it was found that damage growth was present with loads between 75% and 100% maximum load. The damage growth could be characterised by low rise time, high amplitude and medium

to high duration. For coupons with crossply lay-up the damage growth was found for loads between 75% and 100% maximum load with low to medium rise time, high amplitude and medium to high duration. In coupons with angleply lay-up the damage growth characteristics were found for loads between 50% and 100% maximum load with high amplitude, medium to high duration and low to high rise time. These features could not initially be recognised for the quasi-isotropic coupons.

5.2. Recommendations

In order to be able to measure the crack growth in the 90° plies, pictures should also be taken during the first 100 cycles.

The large amount of scatter in the cyclic work and dissipated energy may be caused by the inaccuracy in the displacement measurements. In order to improve this, the accuracy of the displacement measurements have to be improved by using an extensometer during the fatigue tests.

In order to more accurately determine the relation between fatigue life and dissipated energy, more tests are required to see if the relation between fatigue life and total dissipated energy is indeed linear.

Energy dissipation behaves differently at higher stress ratios, therefore in order to investigate the effect of stress ratio on energy dissipation, fatigue tests have to be performed at multiple stress ratios. Increasing the stress ratio could also remove the acoustic emission hits caused by friction based mechanisms, improving the acoustic emission data related to damage growth.

In order to relate the acoustic emission features to the damage mechanisms better, the acoustic emission features could be analysed using pattern recognition software. To compare with the crack growth graph the features could also be sorted using the cycles at which they appear instead of the loads. Because amplitude depends on the distance between sensor and the acoustic event, using frequency based analysis instead of amplitude based analysis could improve the damage characterisation with acoustic emission.

.

Bibliography

[1] L. Amaral, L. Yao, R. Alderliesten, and R. Benedictus. The relation between the strain energy release in fatigue and quasi-static crack growth. *Engineering Fracture Mechanics*, 145:86–97, 2015. doi: 10.1016/j.engfracmech.2015.07.018.

[2] L. Amaral, R. Alderliesten, and R. Benedictus. Understanding mixed-mode cyclic fatigue delamination growth in unidirectional composites: An experimental approach. *Engineering Fracture Mechanics*, 180: 161–178, 2017. ISSN 0013-7944. doi: http://dx.doi.org/10.1016/j.engfracmech.2017.05.049.

[3] L. Amaral, D. Zarouchas, R. Alderliesten, and R. Benedictus. Energy dissipation in mode II fatigue crack growth. *Engineering Fracture Mechanics*, 173:41–54, 2017. doi: 10.1016/j.engfracmech.2017.01.020.

[4] ASTM D5766/D5766M-11. Standard Test Method for Open-Hole Tensile Strength of Polymer Matrix Composite Laminates. Technical report, ASTM, 2011.

[5] H.N. Bar, M.R. Bhat, and C.R.L. Murthy. Parametric analysis of acoustic emission signals for evaluating damage in composites using a pvdf film sensor. *Journal of Nondestructive Evaluation*, 24:121–134, 2005.

[6] A. Belaadi, A. Bezazi, M. Maache, and F. Scarpa. Fatigue in Sisal Fiber Reinforced Polyester Composites: Hysteresis and Energy Dissipation. *Procedia Engineering*, 74:325–328, 2014. ISSN 1877-7058. doi: 10.1016/j.proeng.2014.06.272.

[7] A. P. Bovsunovsky. The mechanisms of energy dissipation in the non-propagating fatigue cracks in metallic materials. *Engineering Fracture Mechanics*, 71(16–17):2271–2281, 2004. ISSN 0013-7944. doi: 10.1016/j.engfracmech.2004.02.003.

[8] W. R. Broughton, M. R. L. Gower, M. J. Lodeiro, G. D. Pilkington, and R. M. Shaw. An experimental assessment of open-hole tension-tension fatigue behaviour of a GFRP laminate. *Composites Part A: Applied Science and Manufacturing*, 42(10):1310–1320, 2011. doi: 10.1016/j.compositesa.2011.05.014.

[9] L. J. Broutman and S. Sahu. A new theory to predict cumulative fatigue damage in fiberglass reinforced plastics. In *Composite materials: Testing and design (second conference)*. ASTM International, 1972.

[10] A. J. Brunner. *Polymer Composites in the Aerospace Industry*, book section Fracture mechanics characterization of polymer composites for aerospace applications, pages 191–230. Elsevier Inc., 2014. doi: 10.1016/B978-0-85709-523-7.00008-6.

[11] A. J. Brunner, S. Stelzer, G. Pinter, and G. P. Terrasi. Cyclic fatigue delamination of carbon fiber-reinforced polymer-matrix composites: Data analysis and design considerations. *International Journal of Fatigue*, 83: 293–299, 2016. doi: 10.1016/j.ijfatigue.2015.10.025.

[12] J. Bär and S. Seifert. Investigation of Energy Dissipation and Plastic Zone Size During Fatigue Crack Propagation in a High-Alloyed Steel. *Procedia Materials Science*, 3:408–413, 2014. ISSN 2211-8128. doi: 10.1016/j.mspro.2014.06.068.

[13] The SciPy Community. scipy.integrate.trapz - SciPy v1.1.0 Reference Guide, September 19 2016. Retrieved from `https://docs.scipy.org/doc/scipy-0.18.1/reference/generated/scipy.integrate.trapz.html`.

[14] Hexcel Corporation. Hexply® 8552 product datasheet (eu version), 2016. Retrieved from `https://www.hexcel.com/user_area/content_media/raw/HexPly_8552_eu_DataSheet.pdf`.

[15] A. D'Amore, M. Giorgio, and L. Grassia. Modeling the residual strength of carbon fiber reinforced composites subjected to cyclic loading. *International Journal of Fatigue*, 78:31–37, 2015. doi: http://dx.doi.org/10.1016/j.ijfatigue.2015.03.012.

[16] A. B. De Morais. Mode I cohesive zone model for delamination in composite beams. *Engineering Fracture Mechanics*, 109:236–245, 2013. doi: 10.1016/j.engfracmech.2013.07.004.

[17] A. B. De Morais. Cohesive zone beam modelling of mixed-mode I-II delamination. *Composites Part A: Applied Science and Manufacturing*, 64: 124–131, 2014. doi: 10.1016/j.compositesa.2014.05.004.

[18] A. B. de Morais and A. B. Pereira. Mode III interlaminar fracture of carbon/epoxy laminates using a four-point bending plate test. *Composites Part A: Applied Science and Manufacturing*, 40(11):1741–1746, 2009. doi: 10.1016/j.compositesa.2009.08.009.

[19] N. ElAgamy, J. Laliberté, and F. Gaidies. Quantitative analysis of fatigue cracks in laminated carbon fibre-reinforced polymer composites using micro-computed tomography. *Journal of Composite Materials*, 50(18): 2523–2540, 2016. doi: 10.1177/0021998315608252.

[20] B. Gozluklu and D. Coker. Modeling of dynamic crack propagation using rate dependent interface model. *Theoretical and Applied Fracture Mechanics*, 85:191–206, 2016. doi: 10.1016/j.tafmec.2016.01.010.

[21] B. G. Green, M. R. Wisnom, and S. R. Hallett. An experimental investigation into the tensile strength scaling of notched composites. *Composites Part A: Applied Science and Manufacturing*, 38(3):867–878, 2007. ISSN 1359-835X.

[22] R. Gutkin, C.J. Green, S. Vangrattanachai, S.T. Pinho, P. Robinson, and P.T. Curtis. On acoustic emission for failure investigation in cfrp: Pattern

recognition and peak frequency analyses. *Mechanical Systems and Signal Processing*, 25:1393–1407, 2011.

[23] M. Janssen, J. Zuidema, and R.J.H. Wanhill. *Fracture Mechanics*. VSSD, 2nd edition, 2006.

[24] A. Kahirdeh and M. M. Khonsari. Energy dissipation in the course of the fatigue degradation: Mathematical derivation and experimental quantification. *International Journal of Solids and Structures*, 77:74–85, 2015. ISSN 0020-7683. doi: 10.1016/j.ijsolstr.2015.06.032.

[25] C. Kassapoglou and M. Kaminski. Modeling damage and load redistribution in composites under tension–tension fatigue loading. *Composites Part A: Applied Science and Manufacturing*, 42(11):1783–1792, 2011. ISSN 1359-835X. doi: http://dx.doi.org/10.1016/j.compositesa.2011.08.001.

[26] H. Mao and S. Mahadevan. Fatigue damage modelling of composite materials. *Composite Structures*, 58(4):405–410, 2002. ISSN 0263-8223. doi: 10.1016/S0263-8223(02)00126-5.

[27] G. Meneghetti. Analysis of the fatigue strength of a stainless steel based on the energy dissipation. *International Journal of Fatigue*, 29(1):81–94, 2007. ISSN 0142-1123. doi: 10.1016/j.ijfatigue.2006.02.043.

[28] G. Meneghetti and M. Ricotta. Evaluating the heat energy dissipated in a small volume surrounding the tip of a fatigue crack. *International Journal of Fatigue*, 92, Part 2:605–615, 2016. ISSN 0142-1123. doi: 10.1016/j.ijfatigue.2016.04.001.

[29] V. Mollón, J. Bonhomme, A. M. Elmarakbi, A. Argüelles, and J. Viña. Finite element modelling of mode i delamination specimens by means of implicit and explicit solvers. *Polymer Testing*, 31(3):404–410, 2012. doi: 10.1016/j.polymertesting.2011.12.008.

[30] A. V. Movahedi-Rad, T. Keller, and A. P. Vassilopoulos. Fatigue damage in angle-ply gfrp laminates under tension-tension fatigue. *International Journal of Fatigue*, 109:60–69, 2018.

[31] P. Naghipour, J. Schneider, M. Bartsch, J. Hausmann, and H. Voggenreiter. Fracture simulation of CFRP laminates in mixed mode bending. *Engineering Fracture Mechanics*, 76(18):2821–2833, 2009. doi: 10.1016/j.engfracmech.2009.05.009.

[32] Q.Q. Ni and M. Iwamoto. Wavelet transform of acoustic emission signals in failure of model composites. *Engineering Fracture Mechanics*, 69:717–728, 2002.

[33] O. J. Nixon-Pearson and S. R. Hallett. An investigation into the damage development and residual strengths of open-hole specimens in fatigue. *Composites Part A: Applied Science and Manufacturing*, 69:266–278, 2015. ISSN 1359-835X. doi: https://doi.org/10.1016/j.compositesa.2014.11.013.

[34] O. J. Nixon-Pearson, S. R. Hallett, P. W. Harper, and L. F. Kawashita. Damage development in open-hole composite specimens in fatigue. Part 2: Numerical modelling. *Composite Structures*, 106:890–898, 2013. ISSN 0263-8223. doi: http://dx.doi.org/10.1016/j.compstruct.2013.05.019.

[35] J. A. Pascoe, R. C. Alderliesten, and R. Benedictus. Methods for the prediction of fatigue delamination growth in composites and adhesive bonds – A critical review. *Engineering Fracture Mechanics*, 112–113:72–96, 2013. ISSN 0013-7944. doi: 10.1016/j.engfracmech.2013.10.003.

[36] J. A. Pascoe, R. C. Alderliesten, and R. Benedictus. Characterising resistance to fatigue crack growth in adhesive bonds by measuring release of strain energy. *Procedia Structural Integrity*, 2:80–87, 2016. ISSN 2452-3216. doi: 10.1016/j.prostr.2016.06.011.

[37] T. P. Philippidis and V. A. Passipoularidis. Residual strength after fatigue in composites: Theory vs. experiment. *International Journal of Fatigue*, 29(12):2104–2116, 2007. ISSN 0142-1123. doi: http://dx.doi.org/10.1016/j.ijfatigue.2007.01.019.

[38] R. B. Pipes, S. V. Kulkarni, and P. V. McLaughlin. Fatigue damage in notched composite laminates. *Materials Science and Engineering*, 30(2):113–120, 1977. ISSN 0025-5416. doi: 10.1016/0025-5416(77)90218-X.

[39] A. Pirondi and F. Moroni. A progressive damage model for the prediction of fatigue crack growth in bonded joints. *Journal of Adhesion*, 86(5-6):501–521, 2010. doi: 10.1080/00218464.2010.484305.

[40] A. Pupurs. *Modeling Damage, Fatigue and Failure of Composite Materials*, book section Fiber failure and debonding in composite materials, pages 175–196. Elsevier Inc., 2015. doi: 10.1016/B978-1-78242-286-0.00009-1.

[41] C. Rans, R. Alderliesten, and R. Benedictus. Misinterpreting the results: How similitude can improve our understanding of fatigue delamination growth. *Composite Science and Technology*, 71:230–238, 2011.

[42] T. Sasikumar, S. RajendraBoopathy, K.M. Usha, and E.S. Vasudev. Failure strength prediction of unidirectional tensile coupons using acoustic emission peak amplitude and energy parameter with artificial neural networks. *Composite Science and Technology*, 69:1151–1155, 2009.

[43] M. R. Satapathy, B. G. Vinayak, K. Jayaprakash, and N. K. Naik. Fatigue behavior of laminated composites with a circular hole under in-plane multiaxial loading. *Materials & Design*, 51:347–356, 2013. ISSN 0261-3069. doi: http://dx.doi.org/10.1016/j.matdes.2013.04.040.

[44] A. Soto, E. V. González, P. Maimí, A. Turon, J. R. Sainz de Aja, and F. M. de la Escalera. Cohesive zone length of orthotropic materials undergoing delamination. *Engineering Fracture Mechanics*, 159:174–188, 2016. doi: 10.1016/j.engfracmech.2016.03.033.

[45] S. Stikkelorum. Raw data, python scripts and analysed data used for investigating energy dissipation for a methodology to fatigue master curves, 2019. TU Delft. Dataset. `http://dx.doi.org/10.4121/uuid:2b9a6683-fc9f-46c7-91d1-b03a30571402`.

[46] Vallen Systeme. Ae-sensor data sheet, 2018. Retrieved from `http://www.vallen.de/fileadmin/user_upload/VS900-M_1512.pdf`.

[47] D. Taylor. The theory of critical distances. *Engineering Fracture Mechanics*, 75(7):1696–1705, 2008. ISSN 0013-7944. doi: http://dx.doi.org/10.1016/j.engfracmech.2007.04.007.

[48] D. Taylor. The Theory of Critical Distances: A link to micromechanisms. *Theoretical and Applied Fracture Mechanics*, 2017. ISSN 0167-8442. doi: https://doi.org/10.1016/j.tafmec.2017.05.018.

[49] D. Tsamtsakis, M. Wevers, and P. de Meester. Acoustic emission from cfrp laminates during fatigue loading. *Journal of Reinforced Plastics and Composites*, 17:1185–1201, 1998.

[50] H. Ullah, A. R. Harland, T. Lucas, D. Price, and V. V. Silberschmidt. Finite-element modelling of bending of CFRP laminates: Multiple delaminations. *Computational Materials Science*, 52(1):147–156, 2012. doi: 10.1016/j.commatsci.2011.02.005.

[51] B. G. Vinayak, K. Jayaprakash, and N. K. Naik. Fatigue behavior of laminated composites with a circular hole under in-plane uniaxial random loading. *Materials & Design*, 40:245–256, 2012. ISSN 0261-3069. doi: http://dx.doi.org/10.1016/j.matdes.2012.03.044.

[52] L. Yao, R.C. Alderliesten, M. Zhao, and R. Bendedictus. Discussion on the use of the strain energy release rate for fatigue delamination characterization. *Composites Part A: Applied Science and Manufacturing*, 66:65–72, 2014.